JEM Journal of Experimental Medicine

ARTICLE

RIPK1 S161 phosphorylation promotes further autophosphorylation and cecal necroptosis in TNF-treated mice

Tao Han[1*], Chenchen Ruan[1*], Huiyong Lin[1], Yuxia Zhang[1], Lang Li[1], Ye-hsuan Sun[1], Chuan-Qi Zhong[1], Xin Chen[1], Kai Huang[1], Yating Cao[1], Zusen Fan[2], Hongbing Zhang[3], Jiahuai Han[1,4,5], and Yingying Zhang[1]

Excess TNF causes systemic inflammatory response syndrome and mortality. RIPK1 coordinates TNF signaling through kinase-dependent and -independent mechanisms. S161 autophosphorylation is a primary function of RIPK1 kinase activity *in vitro*, and here we show that it is sufficient to mediate RIPK1 kinase–dependent function *in vivo*. S161 phospho-mimic mutation (S161E) effectively overcomes chemical or genetic inhibition of RIPK1 kinase activity in TNF-treated cells and mice. Mechanistically, S161 autophosphorylation is necessary for further autophosphorylation in RIPK1, including at S166. *Ripk1*$^{S161E/S161E}$ mice are hypersensitive to TNF, enabling us to observe low-dose TNF-induced necroptosis in cecal intestinal epithelial cells (IECs) and endothelial cells (ECs) and uncover a reciprocal enhancement between IEC and EC necroptosis and a selective increase of IL-6 in the circulation by necroptosis. IL-6 promotes cecal edema and synergizes with IEC and EC necroptosis, causing cecal damage and mouse death. Our data elucidate a mechanism of RIPK1 kinase–dependent function in TNF signaling and its role in cecal pathology and mouse mortality.

Introduction

TNF-α (TNF) plays a pivotal role in orchestrating inflammatory responses. It can promote inflammation directly by inducing inflammatory gene expression or indirectly by triggering cell death to release damage-associated molecular patterns (DAMPs). Apoptosis and necroptosis are two types of programmed cell death induced by TNF. TNF-induced necroptosis is mediated by the activation of receptor-interacting serine/threonine-protein kinase 1 (RIPK1) and RIPK3 to form the necrosome, followed by mixed-lineage kinase domain-like (MLKL) oligomerization and translocation into the plasma membrane (Cho et al., 2009; Degterev et al., 2008; He et al., 2009; Holler et al., 2000; Sun et al., 2012; Zhang et al., 2009; Zhang et al., 2018). In many contexts, caspase-8 suppresses necroptosis, and the induction of its auto-processing leads to apoptosis and diseases. The competition and switch between TNF-induced necroptosis and apoptosis have been revealed by numerous *in vitro* and *in vivo* studies (Schwarzer et al., 2020b). RIPK1 not only serves as a scaffold in complex I to promote the activation of the nuclear factor-kappa B (NF-κB) and mitogen-activated protein kinase (MAPK) pathways but also forms an important component in complex II to promote programmed cell death (Zhang et al., 2018). Posttranslational modifications of RIPK1, such as phosphorylation, ubiquitination, and oxidation, enable it to carry out its diverse functions under different conditions (Mifflin et al., 2020). Several single amino acid mutations in RIPK1, such as K115R, K376R, and K612R, have been proven to be disease associated in animal models (Kist et al., 2021; Li et al., 2020; Tang et al., 2019; Tu et al., 2021; Zhang et al., 2019b), while RIPK1 D324N/H/Y/V mutations have been verified to cause diseases in human patients (Lalaoui et al., 2020; Tao et al., 2020). RIPK1 can exert functions as a kinase or a scaffold, and its kinase activity has been implicated in the progression of several diseases (Mifflin et al., 2020), making RIPK1 a promising therapeutic target in clinical trials for diseases such as rheumatoid arthritis and ulcerative colitis (Weisel et al., 2021a; Weisel et al., 2021b). Serine 166 (S166) phosphorylation is a widely used marker for RIPK1 activation, while S25 and Y383 are inhibitory phosphorylation sites in RIPK1, the roles of which

[1]State Key Laboratory of Cellular Stress Biology, School of Life Sciences, Faculty of Medicine and Life Sciences, Xiamen University, Xiamen, China; [2]Key Laboratory of RNA Science and Engineering, Key Laboratory of Epigenetic Regulation and Intervention, Institute of Biophysics, Chinese Academy of Sciences, Beijing, China; [3]Department of Physiology, State Key Laboratory of Common Mechanism Research for Major Diseases, Haihe Laboratory of Cell Ecosystem, Institute of Basic Medical Sciences and School of Basic Medicine, Chinese Academy of Medical Sciences and Peking Union Medical College, Beijing, China; [4]Research Unit of Cellular Stress of Chinese Academy of Medical Science, Xiang'an Hospital of Xiamen University, Cancer Research Center of Xiamen University, School of Medicine, Faculty of Medicine and Life Sciences, Xiamen University, Xiamen, China; [5]Laboratory Animal Center, Faculty of Medicine and Life Sciences, Xiamen University, Xiamen, China.

*T. Han and C. Ruan contributed equally to this paper. Correspondence to Jiahuai Han: jhan@xmu.edu.cn; Yingying Zhang: y.zhang@xmu.edu.cn.

have all been shown in several mouse disease models (Dondelinger et al., 2019; Laurien et al., 2020; Tu et al., 2022). However, the *in vivo* role of S161, an important autophosphorylation site for RIPK1 to function in necroptosis (Zhang et al., 2017), and the relationship between phosphorylation of S161 and other sites in RIPK1 function are unclear.

TNF is one of the few cytokines that, by itself, is sufficient to induce systemic inflammatory response syndrome (SIRS). SIRS is an exaggerated defense response of the body to a noxious stressor to localize and then eliminate the source of the insult (infection or trauma, etc.) (Chakraborty and Burns, 2024). Even though the purpose is defensive, the dysregulated response can cause a massive inflammatory cascade, leading to reversible or irreversible organ dysfunction and even death (Chakraborty and Burns, 2024; Huyghe et al., 2023; Tracey et al., 1986). Studies using mouse models suggest that TNF-induced necroptosis is the central mediator of SIRS (Chen et al., 2015; Duprez et al., 2011; Newton et al., 2016; Newton et al., 2014). Interestingly, the cecum was found to be the most sensitive organ to TNF-induced injury, and necroptosis of intestinal epithelial cells (IECs) is the major cause of the cecal damage (Chen et al., 2015; Newton et al., 2016; Wu et al., 2024a). Furthermore, we recently reported that surgical removal of the cecum (cecectomy) prevents TNF-induced mouse death. The observed animal death results from cardiac dysfunction triggered by cecal damage, demonstrating that necroptosis in the cecum is an essential early event in TNF-induced SIRS and animal death (Wu et al., 2024a). However, detailed mechanisms of necroptosis in the cecum are not fully elucidated.

IL-6 is an important inflammatory cytokine, which can be induced by various stimuli, including TNF (De Cesaris et al., 1998; Hunter and Jones, 2015). Blocking IL-6 using anti–IL-6 antibodies or IL-6 KO has been shown to protect mice from SIRS (Libert et al., 1992; Sundgren-Andersson et al., 1998). However, the systemic administration of recombinant IL-6 alone does not cause detrimental effects in mice (Leuchtmann et al., 2022; Liu et al., 1992; Mulé et al., 1992). In addition, although the RIPK1 non-cleavable mutant (D325A in mice and D324N/H/Y/V in human patients) triggers cell death mediated by TNF (Lalaoui et al., 2020; Newton et al., 2019; Tao et al., 2020; Zhang et al., 2019a; Zhang et al., 2021), patients responded to tocilizumab, a monoclonal antibody against IL-6R, but did not respond to TNF inhibitors (Lalaoui et al., 2020; Tao et al., 2020). Therefore, how circulating IL-6 participates in SIRS is an intriguing question that remains unanswered.

By utilizing a series of mouse strains, including mice carrying the RIPK1 S161 to Glu (E), Asn (N), or Ala (A) mutation, and the S161 to E mutation in a RIPK1 kinase–dead background, this study demonstrated an important role of RIPK1 autophosphorylation at S161 in TNF-induced mouse death. Mimicking S161 phosphorylation enhances necroptosis of IECs and endothelial cells (ECs) in the cecum, which reinforces each other, leading to cecal damage. The necroptosis of IECs and ECs, rather than that of hematopoietic cells, is the primary driver of TNF-induced SIRS. In addition, the autophosphorylation of RIPK1 at S161 and S166 is most likely a sequential event. As our data showed, mimicking S161 phosphorylation could lead to phosphorylation at S166 but not vice versa. Exploring the pathology of TNF-treated *Ripk1*$^{S161E/S161E}$ mice revealed that IL-6 is the major cytokine elicited by necroptosis, which contributes to TNF-induced mouse death. Overall, our work demonstrated the critical role of RIPK1 S161 autophosphorylation in necroptosis and its potential role in initiating a chain reaction of RIPK1 autophosphorylation and elucidated how RIPK1-RIPK3-mediated IEC and EC necroptosis leads to TNF-triggered cecal damage and subsequent mouse death.

Results

RIPK1 S161 phosphorylation is important for TNF-induced lethality in mice

To study the physiopathological roles of RIPK1 S161 phosphorylation, we generated three mouse strains with genotypes of *Ripk1*$^{S161E/S161E}$, *Ripk1*$^{S161N/S161N}$, or *Ripk1*$^{S161A/S161A}$. All mutant mice were viable, fertile, and healthy and were born at expected Mendelian ratios when inbreeding heterozygous mice (Fig. S1, A–C), suggesting that phosphorylation of RIPK1 at S161 is not required for normal development. To assess the role of RIPK1 S161 phosphorylation in RIPK1-mediated pathogenesis, we utilized a TNF-induced SIRS model (Chakraborty and Burns, 2024; Tracey et al., 1986; Wu et al., 2024a). As expected, the phospho-mimic (*Ripk1*$^{S161E/S161E}$) mice were more sensitive to TNF-induced death than WT mice (Fig. 1 A). Both *Ripk1*$^{S161N/S161N}$ and *Ripk1*$^{S161A/S161A}$ mice harbor S161 phospho-resistant RIPK1. As we described previously (Zhang et al., 2017), based on the crystal structure and structural modeling, the asparagine in the S161N mutant could help maintain a closed RIPK1 structure by forming hydrogen bonds with the carboxyl oxygen of D156, similar to the hydrogen bonds between S161 and D156 (Xie et al., 2013). Consistent with our observations in cell-based studies (Zhang et al., 2017), *Ripk1*$^{S161N/S161N}$ mice were resistant to TNF-induced death (Fig. 1 B). Different from the N mutation, the RIPK1 S161A mutation weakens the interaction between amino acid 161 and D156, thereby increasing the flexibility of the T-loop (Xie et al., 2013). This may explain why *Ripk1*$^{S161A/S161A}$ mice displayed sensitivity to TNF similar to that of WT mice (Fig. 1 B), which is also in line with the cell-based data that the S161A mutation only slightly reduces TNF-induced necroptosis (Degterev et al., 2008; McQuade et al., 2013; Zhang et al., 2017). Consistently, bone marrow–derived macrophages (BMDMs) from *Ripk1*$^{S161E/S161E}$ mice were more sensitive, while *Ripk1*$^{S161N/S161N}$ BMDMs were more resistant to TNF + z-VAD-FMK (zVAD) as well as TNF + second mitochondrial-derived activator of caspases (SMAC) mimetic + Emricasan (TSE)-induced necroptosis (Fig. S1 D). Notably, the inhibition of the S161N mutation on TSE-induced cell death was less effective than that on TNF + zVAD-induced death of BMDMs. Further investigation revealed that the LD_{100} of TNF in inducing death of *Ripk1*$^{S161E/S161E}$ mice is ∼50 µg/kg (Fig. 1 C), which is nearly one order of magnitude lower than that in WT mice (Annibaldi et al., 2018; Dondelinger et al., 2019; Günther et al., 2011; Laurien et al., 2020; Newton et al., 2016; Newton et al., 2014; Newton et al., 2019). Collectively, our data

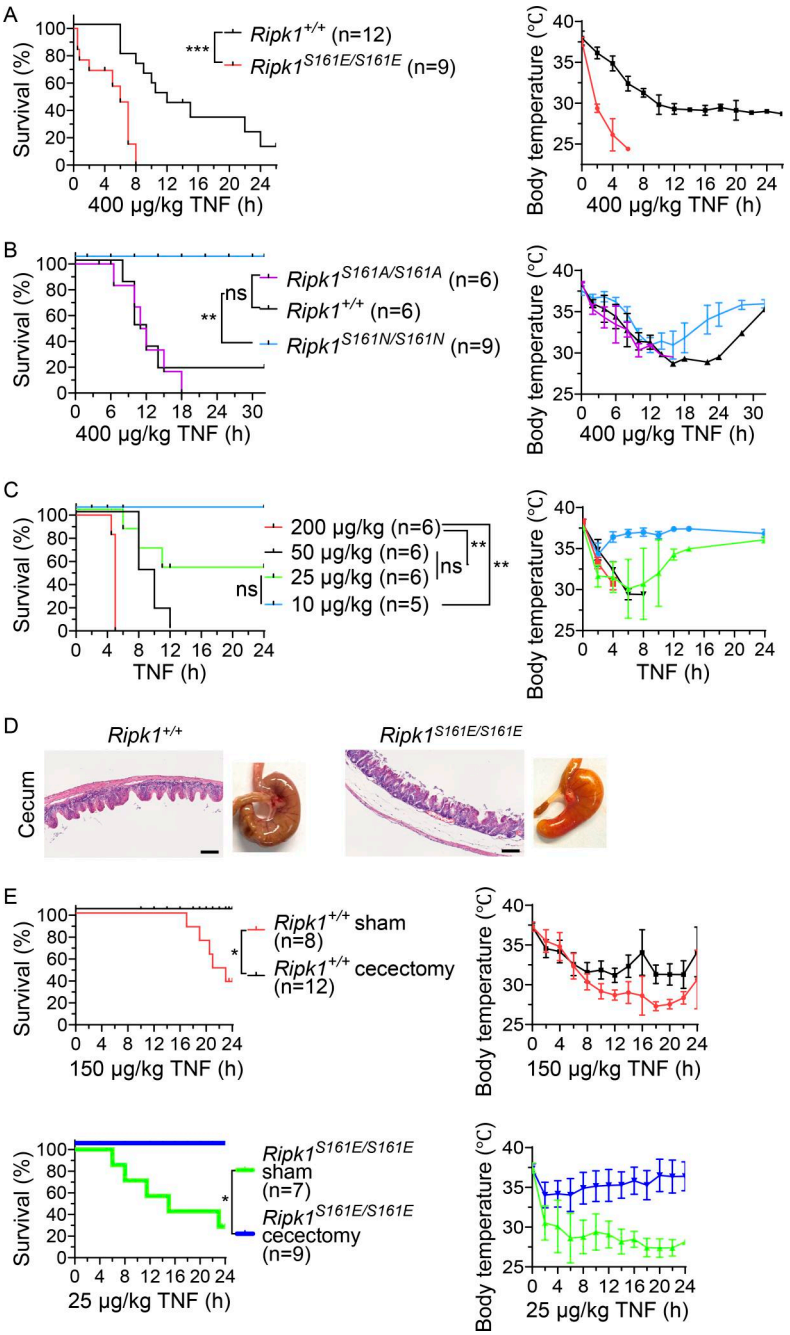

Figure 1. **RIPK1 S161 phosphorylation sensitizes the cecum to TNF-induced damage and is important for TNF-induced lethality in mice. (A and B)** Survival curves and body temperature of 8- to 12-wk-old male littermate mice of the indicated genotypes after TNF injection (400 μg/kg, i.v.). **(C)** Survival curves and body temperature of 8- to 12-wk-old male littermate *Ripk1*$^{S161E/S161E}$ mice after i.v. injection with TNF of the indicated doses. **(D)** Representative photos and H&E staining images of ceca from three mice of each indicated genotype (50 μg/kg TNF treated for 6 h, i.v.). Scale bars, 100 μm. All mice were 8- to 12-wk-old male littermates. **(E)** 6- to 8-wk-old male littermate mice were treated with or without cecectomy and then injected with TNF after 4 wk (150 μg/kg i.v. for *Ripk1*$^{+/+}$ mice and 25 μg/kg i.v. for *Ripk1*$^{S161E/S161E}$ mice). Survival curve is presented as a Kaplan–Meier plot, and the log-rank (Mantel–Cox) test (two-sided) is performed to determine statistical significance. ns, $P \geq 0.05$; *$P < 0.05$; **$P < 0.01$; ***$P < 0.001$. Data of body temperature are presented as mean ± SD. The above experiments were independently performed twice. All mice used in this work were on a C57BL/6 background.

demonstrate that RIPK1 S161 phosphorylation promotes TNF-induced death in mice.

S161E mutation sensitizes the cecum to TNF-induced damage

The cecum is the most sensitive organ to TNF in WT mice (Chen et al., 2015; Wu et al., 2024a). To elucidate the target site(s) of S161E sensitization, tissues from TNF-treated WT and *Ripk1*$^{S161E/S161E}$ mice were collected and examined. The ceca of 50 μg/kg of TNF-treated *Ripk1*$^{S161E/S161E}$ mice showed severe hyperemia, edema, and damage in the villi (Fig. 1 D) to an extent similar to that in LD_{100} dose of TNF-challenged WT mice (400 μg/kg, Fig. S1 E) (Chen et al., 2015; Wu et al., 2024a). In contrast, no obvious abnormalities were observed in the liver, spleen, lung, or kidney (Fig. S1 F). As cecectomy has been successfully applied to rescue TNF-induced SIRS in WT mice (Wu et al., 2024a), we also performed cecectomy and found that it indeed completely protected *Ripk1*$^{S161E/S161E}$ mice from 25 μg/kg of TNF-induced hypothermia and death (the LD_{50} dose, Fig. 1 E). However, cecectomy cannot protect *Ripk1*$^{S161E/S161E}$ mice from LD_{100} dose (50 μg/kg) of TNF-induced lethality (Fig. S1 G), suggesting that some other organs/tissues are also sensitized to TNF-induced damages by the S161E mutation. Collectively, these data revealed that the S161E mutation enhances TNF-induced mortality by sensitizing some organs/tissues to TNF-induced damage, and the cecum is the primarily sensitized organ.

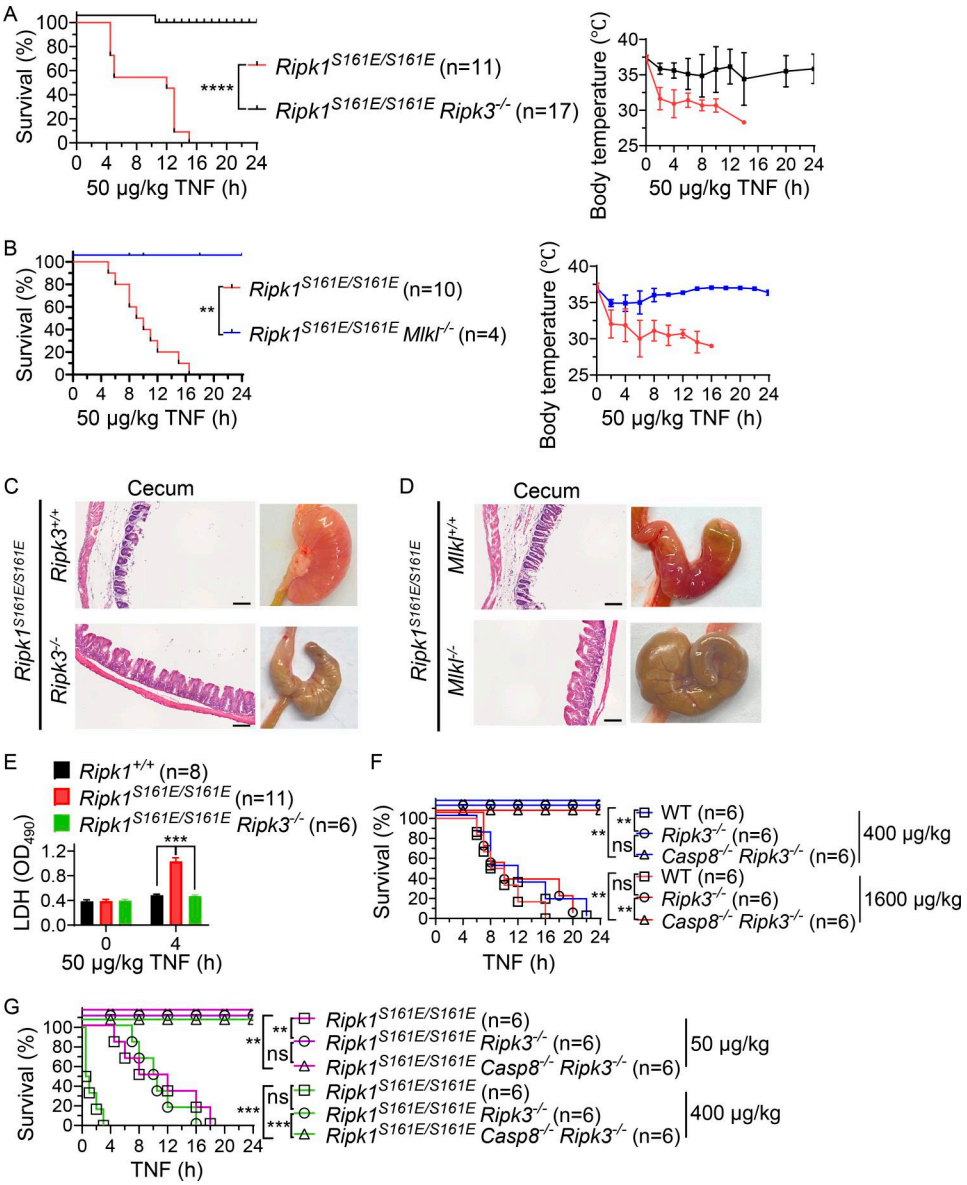

Figure 2. **The necroptotic pathway plays a primary role in TNF-induced death of *Ripk1*$^{S161E/S161E}$ mice. (A and B)** Survival curves and body temperature of 8- to 12-wk-old male littermate mice of the indicated genotypes after TNF injection (50 μg/kg, i.v.). **(C and D)** Representative photos and H&E staining images of ceca from three mice of each indicated genotype (50 μg/kg TNF treated for 6 h, i.v.). Scale bars, 100 μm. **(E)** Mice of the indicated genotypes were i.v. injected with TNF (50 μg/kg). At the indicated time points, serum samples were collected for measurements of LDH. Data are presented as mean ± SD. P values are determined by a two-tailed, unpaired *t* test. ***P < 0.001. All mice were 8- to 12-wk-old male littermates (C–E). **(F and G)** Survival curves of 8- to 12-wk-old male littermate mice of the indicated genotypes after i.v. injection with TNF of the indicated doses. Mouse survival is presented as a Kaplan–Meier plot, and the log-rank test is performed. ns, P ≥ 0.05; **P < 0.01; ***P < 0.001; ****P < 0.0001. Data of body temperature are presented as mean ± SD. The above experiments were independently performed twice.

The hypersensitivity of *Ripk1*$^{S161E/S161E}$ mice to TNF-induced death is due to the increased susceptibility to TNF-induced RIPK1 kinase activity–dependent cell death

Necroptosis plays an essential role in TNF-induced SIRS in mice (Chen et al., 2015; Duprez et al., 2011; Newton et al., 2016; Newton et al., 2014). To gain insights into the enhancement of SIRS in *Ripk1*$^{S161E/S161E}$ mice, *Ripk1*$^{S161E/S161E}$ mutant mice were crossed to *Ripk3*$^{-/-}$ or *Mlkl*$^{-/-}$ background. The lethality, hypothermia, and cecal damage of *Ripk1*$^{S161E/S161E}$ mice resulting from 50 μg/kg of TNF insult were rescued by *Ripk3* or *Mlkl* KO (Fig. 2, A–D), demonstrating the involvement of the necroptosis pathway. In support of this conclusion, TNF-induced release of lactate dehydrogenase (LDH) into the blood, an indicator of cell necrosis (Chan et al., 2013), was higher in *Ripk1*$^{S161E/S161E}$ mice compared with WT mice and was abolished by *Ripk3* deletion (Fig. 2 E). Thus, the low-dose (50 μg/kg) TNF-induced death of *Ripk1*$^{S161E/S161E}$ mice is primarily mediated by the necroptosis pathway.

Since intestinal IEC deletion of *Casp8* leads to spontaneous colitis, it is believed that the primary role of caspase-8 in IECs is

to block necroptosis (Günther et al., 2011; Schwarzer et al., 2020a). However, caspase-8 also has a promoting role in TNF-induced SIRS and animal death (Newton et al., 2016). Most likely due to pathway complementation/compensation, cross talk, or perhaps other network regulations (Holler et al., 2000; Huyghe et al., 2023; Schwarzer et al., 2020b; Zhang et al., 2009), we could observe that an LD_{100} dose (400 μg/kg) of TNF-induced death of WT mice can be blocked by *Ripk3* deletion, but a dose of 1,600 μg/kg of TNF-induced death of WT mice can only be blocked by *Ripk3* and *Casp8* double KO (Fig. 2 F). Similar phenomenon was observed in $Ripk1^{S161E/S161E}$ mice, as *Ripk3* deletion can prevent low-dose (50 μg/kg) TNF-induced death of $Ripk1^{S161E/S161E}$ mice, but only a concomitant loss of *Ripk3* and *Casp8* can block the death from a 400 μg/kg dose of TNF treatment (Fig. 2 G). Therefore, it seems that S161E also sensitizes cells to caspase-8–mediated death in *Ripk3* KO mice.

We then sought to evaluate whether the S161E mutation can enhance apoptosis. CT26 is a murine IEC cell line that lacks RIPK3 expression and can undergo TNF + SMAC mimetic-induced RIPK1 kinase activity–dependent apoptosis (Dondelinger et al., 2013; Dondelinger et al., 2015; Wang et al., 2008) and TNF + cycloheximide (CHX)-induced RIPK1 kinase activity–independent apoptosis (Dondelinger et al., 2015; Van Antwerp et al., 1996). We generated *Ripk1* KO CT26 cell line and reconstituted *Ripk1* expression with WT, kinase-dead (K45A+K46T, KK-AT), S161E, KK-AT + S161E, or S161N RIPK1. As shown in Fig. S2 A, TNF alone did not lead to cell death in all of these cells; TNF + SMAC mimetic-induced cell death was blocked by KK-AT or S161N mutation and was not affected by S161E and KK-AT + S161E. These data confirmed that TNF + SMAC mimetic-induced CT26 death is RIPK1 kinase activity–dependent apoptosis and further pointed out that this apoptosis requires S161 phosphorylation, and S161E mutation can bypass the RIPK1 kinase activity blockade by KK-AT mutation to mediate apoptosis. In contrast, TNF + CHX-induced cell death was not influenced by any of these mutations (Fig. S2 A). Although BMDMs have *Ripk3* expression, TNF + SMAC mimetic and TNF + CHX can induce RIPK1 kinase–dependent and –independent apoptosis, respectively, in these cells (Berger et al., 2014; Dondelinger et al., 2013; Dondelinger et al., 2015; Polykratis et al., 2014; Van Antwerp et al., 1996; Wang et al., 2008). WT, $Ripk1^{K45A/K45A}$, $Ripk1^{S161E/S161E}$, $Ripk1^{K45A+S161E/K45A+S161E}$, $Ripk1^{S161N/-S161N}$, and $Ripk1^{S161A/S161A}$ primary BMDMs were derived from mice and subjected to the same treatments as in Fig. S2 A, and similar results were obtained, which were not affected by the addition of the RIPK3 inhibitor, GSK-872 (Fig. S2, B–D). Collectively, our data indicated that S161 phosphorylation is also a primary function of RIPK1 kinase activity in RIPK1 kinase activity–dependent apoptosis. Thus, we concluded that S161 phosphorylation is the primary function of RIPK1 kinase activity in RIPK1 kinase activity–dependent cell death, including necroptosis and apoptosis, and this is the underlying mechanism of the increased sensitivity of $Ripk1^{S161E/S161E}$ mice to TNF-induced death.

RIPK1 autophosphorylation at S161 promotes further phosphorylation at other sites of RIPK1, including S166

Necroptosis is mediated by a supermolecular complex called necrosome, which consists of RIPK1, RIPK3, Fas-associated death domain (FADD), and MLKL (Cho et al., 2009; Degterev et al., 2008; He et al., 2009; Holler et al., 2000; Sun et al., 2012; Zhang et al., 2009). Consistent with the above *in vivo* study, the RIPK1 phospho-mimic mutation S161E led to more RIPK3 recruitment to necrosomes in L929 cells, whereas the phosphorylation-unresponsive S161N mutation prevented necrosome formation (Fig. 3 A). Stochastic optical reconstruction microscopy (STORM) super-resolution imaging analysis supported that more RIPK3 were recruited and larger necrosomes with more RIPK3 molecules were formed in cells expressing the RIPK1 S161E mutant than in the control cells (Fig. 3 B and Fig. S3 A).

Besides S161, several other phosphorylation sites in RIPK1 have been identified (Degterev et al., 2008; Dondelinger et al., 2019; Dondelinger et al., 2017; Grimsrud et al., 2012; Jaco et al., 2017; Jetton et al., 2024; Laurien et al., 2020; Menon et al., 2017; Shutinoski et al., 2016; Tu et al., 2022; Wu et al., 2020; Zhang et al., 2017), among which S166 is frequently addressed (Jetton et al., 2024; Laurien et al., 2020; McQuade et al., 2013). Intriguingly, we detected S166 phosphorylation in the RIPK1 S161E mutant expressed *Ripk1* KO L929 cells without any stimulation (Fig. 3 C). An involvement of autocrine TNF was excluded by the addition of anti-TNF antibodies (Fig. S3 B). S166 phosphorylation was also detected in primary MEFs, cecal IECs, and primary BMDMs from $Ripk1^{S161E/S161E}$ mice in the absence of stimulation (Fig. 3, D and E; and Fig. S3 C). These observations raise the possibility that S161 autophosphorylation leads to S166 autophosphorylation. Notably, a band shift occurred in the RIPK1 S161E mutant reconstituted L929 cells following a necroptotic stimulation (Fig. 3 C), indicating that other modifications might have occurred upon TNF treatment but not in the steady state.

To better understand the effect of RIPK1 S161 phosphorylation on other phosphorylation events of RIPK1, we analyzed RIPK1 phosphorylation in unstimulated *Ripk1* KO L929 cells reconstituted with WT RIPK1 or RIPK1 S161E mutant and TNF + zVAD (a pan-caspase inhibitor)-stimulated WT RIPK1-reconstituted cells by mass spectrometry (MS). Several reported phosphorylation sites of RIPK1 were detected (Degterev et al., 2008; Dondelinger et al., 2019; Laurien et al., 2020; Menon et al., 2017; Sacco et al., 2016; Shutinoski et al., 2016; Wu et al., 2020), with some of these sites, including S166, revealed to be phosphorylated in an S161E-dependent manner (Fig. 3 F). Some reported sites, such as T169, were not detected in this analysis, possibly owing to variations in methodology. Since S166 is known as a TNF-inducible phosphorylation site (Dondelinger et al., 2019; Laurien et al., 2020), we proposed that TNF-induced RIPK1 autophosphorylation at S161 initiates the phosphorylation of S166 and possibly other sites.

To test this hypothesis, we reconstituted RIPK1 S161N, S161E, S161E + S166A, S161A, or the kinase-dead KK-AT mutant in *Ripk1* KO L929 cells and assessed S166 phosphorylation and cell death before and after TNF + zVAD treatment (Fig. 3 G). As expected, the KK-AT mutant abolished S166 phosphorylation and cell death. Unlike the presence of steady-state and induced S166 phosphorylation in S161E mutant cells and the enhanced cell death by the S161E mutation, the S161N mutation prevented both the steady-state and TNF-induced S166 phosphorylation and cell

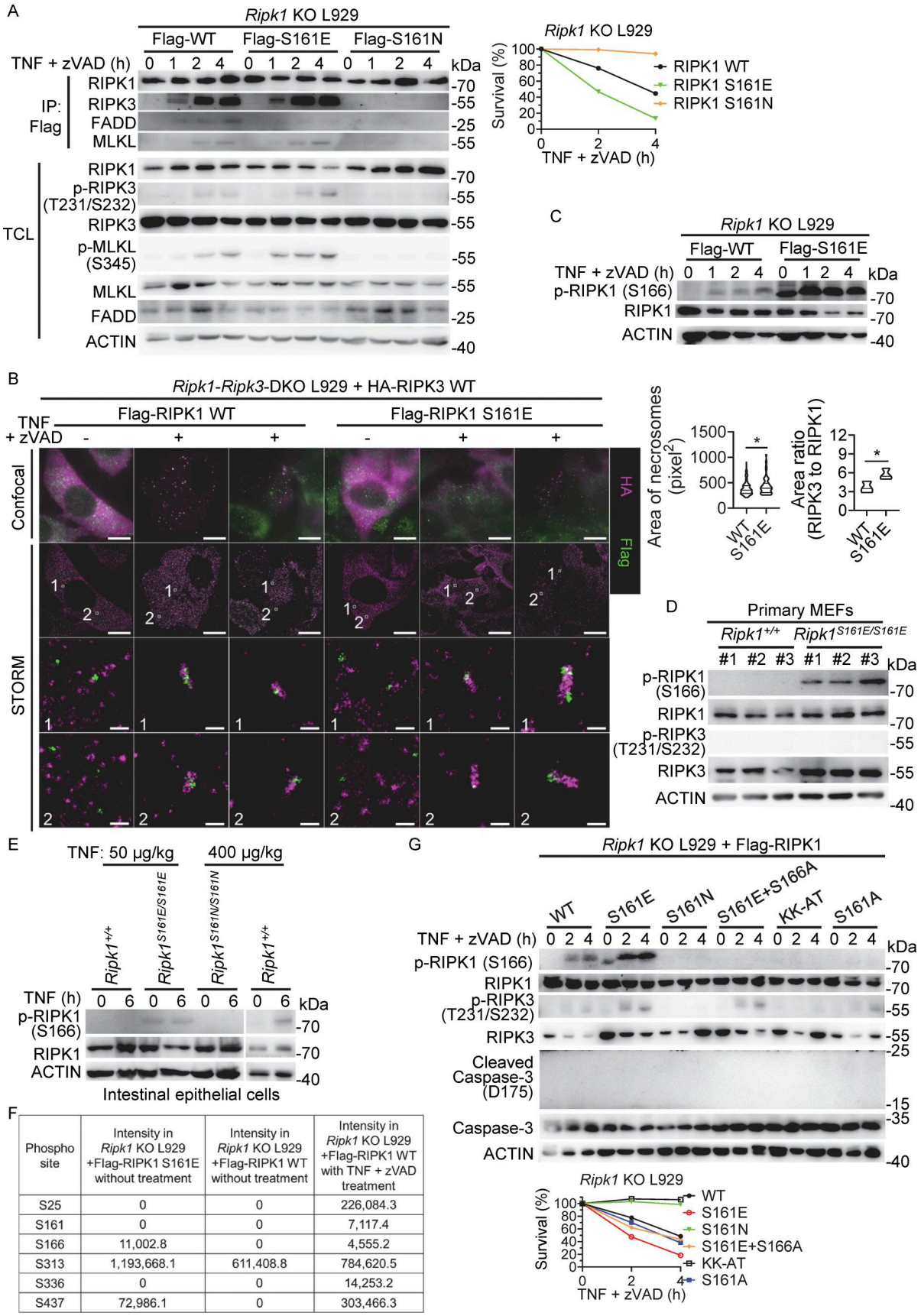

Phospho site	Intensity in *Ripk1* KO L929 +Flag-RIPK1 S161E without treatment	Intensity in *Ripk1* KO L929 +Flag-RIPK1 WT without treatment	Intensity in *Ripk1* KO L929 +Flag-RIPK1 WT with TNF + zVAD treatment
S25	0	0	226,084.3
S161	0	0	7,117.4
S166	11,002.8	0	4,555.2
S313	1,193,668.1	611,408.8	784,620.5
S336	0	0	14,253.2
S437	72,986.1	0	303,466.3

Figure 3. **RIPK1 phosphorylation at S161 occurs prior to RIPK1 phosphorylation at S166. (A)** *Ripk1*-deficient L929 cells were reconstituted with Flag-RIPK1 WT, S161E, or S161N mutant and then treated with TNF (10 ng/ml) + zVAD (20 μM) for the indicated time points. Cell survival was measured. Cell lysates were

immunoprecipitated (IP) with anti-Flag M2 beads. Total cell lysates (TCL) and IP samples were analyzed by immunoblotting with antibodies as indicated. **(B)** *Ripk1* and *Ripk3* double-deficient L929 cells were reconstituted with Flag-RIPK1 WT or S161E mutant and HA-RIPK3 WT and then treated with TNF (10 ng/ml) + zVAD (20 μM) for 2.5 h. Representative confocal and STORM images from two independent experiments of RIPK1 (green) and RIPK3 (purple) in L929 cells with or without treatment are shown. Scale bars, 10 μm for the first and second rows and 200 nm for the third and fourth rows from the top. Area of necrosomes formed after treatment and area ratios of RIPK3 to RIPK1 were analyzed using ImageJ. P values are determined by a two-tailed, unpaired *t* test. *P < 0.05. **(C)** *Ripk1*-deficient L929 cells were reconstituted with Flag-RIPK1 WT or S161E mutant and then treated with TNF (10 ng/ml) + zVAD (20 μM) for the indicated time points. Cell lysates were analyzed by immunoblotting to detect proteins as indicated. **(D)** Cell lysates of nontreated primary MEFs from full-sibling $Ripk1^{+/+}$ and $Ripk1^{S161E/S161E}$ embryos were analyzed by immunoblotting. Each number represents one embryo. **(E)** IECs from 8- to 12-wk-old male littermate $Ripk1^{+/+}$, $Ripk1^{S161E/S161E}$, and $Ripk1^{S161N/S161N}$ mice injected with PBS or TNF for 6 h were isolated (50 μg/kg of TNF for $Ripk1^{S161E/S161E}$ mice and $Ripk1^{+/+}$ controls, 400 μg/kg of TNF for $Ripk1^{S161N/S161N}$ mice and $Ripk1^{+/+}$ controls). Cell lysates were subjected to immunoblotting. **(F)** Intensities of RIPK1 phosphorylation sites measured by LC–MS/MS. Samples were those in C without or with treatment. **(G)** *Ripk1*-deficient L929 cells were reconstituted with Flag-RIPK1 WT or mutants (S161E, S161N, S161E + S166A, S161A, and the kinase-dead mutant KK-AT) and then treated with TNF (10 ng/ml) + zVAD (20 μM) for the indicated time points. Cell survival was measured. Cell lysates were analyzed by immunoblotting. Data are presented as mean ± SD of triplicate. The above experiments were independently performed twice. Source data are available for this figure: SourceData F3.

death (Fig. 3 G). Notably, the S161A mutation prohibited S166 phosphorylation, even at a late time point when a large number of cells had died (Fig. 3 G). The specificity of the anti–phospho-S166 antibody was confirmed by the lack of phospho-S166 in RIPK1 S161E + S166A-reconstituted *Ripk1* KO L929 cells, and the occurrence of necroptosis was confirmed by the detection of phospho-RIPK3 (Fig. 3 G). Analyses of the S166 phosphorylation and death pathway activation in WT, $Ripk1^{S161E/S161E}$, $Ripk1^{S161N/S161N}$, $Ripk1^{K45A/K45A}$, and $Ripk1^{S161A/S161A}$ BMDMs showed similar results to that in Fig. 3 G (Fig. S3 D). Thus, S161 phosphorylation appears to be a prerequisite for S166 phosphorylation in L929 cells and BMDMs.

The role of S166 phosphorylation has been demonstrated by the S166A mutation *in vitro* and *in vivo* (Laurien et al., 2020). Perhaps due to the structural flexibility similar to the S161A mutant (Xie et al., 2013; Zhang et al., 2017), the S166A mutation did not completely block necroptosis (Fig. S3 E) (Laurien et al., 2020). We then generated the S166N mutant and found that its expression in *Ripk1* KO L929 cells is a complete loss-of-function in mediating TNF-induced necroptosis (Fig. S3 E). To test if S166 phosphorylation could lead to S161 phosphorylation, we analyzed RIPK1 phosphorylation in unstimulated *Ripk1* KO L929 cells reconstituted with RIPK1 S166E mutant as we did in Fig. 3 F and found that the S166E mutation does not cause S161 phosphorylation (Fig. S3 F). Additionally, the phospho-mimic S166E mutant cannot even efficiently mediate TNF-induced necroptosis (Fig. S3 E). A band shift of phospho-RIPK1 S166 was observed after TNF treatment in S161E-reconstituted L929 cells (Fig. 3, C and G) but not in BMDMs (Fig. S3 D) or IECs (Fig. 3 E), showing the presence of other cell type–dependent modifications in RIPK1. Thus, while the phosphorylation of S161, phosphorylation of S166, and possibly other modifications may all contribute to RIPK1-dependent necroptosis, S161 is unique among them since currently only the S161E mutation shows a gain-of-function in efficiently driving TNF-induced necroptosis in L929 cells in a systematic analysis (Zhang et al., 2017). Collectively, these data support the notion that S161 autophosphorylation is a driver for further autophosphorylation in RIPK1 and is one of the determinants of TNF-induced necroptosis.

Mimicking S161 phosphorylation can compensate for the loss of RIPK1 kinase activity in initiating TNF-induced mouse death

It is known that RIPK1 kinase activity is required for TNF-induced necroptosis (Berger et al., 2014; Kaiser et al., 2014; Newton et al., 2014; Polykratis et al., 2014), and our previous study showed that the S161E mutation can bypass the kinase-dead mutation in RIPK1 to transduce the signal of necroptosis in cultured cells (Zhang et al., 2017). To evaluate whether the S161 phosphorylation can compensate for the loss of RIPK1 kinase activity to mediate mouse death, an additional RIPK1 kinase–dead mutation (K45A) was introduced into the $Ripk1^{S161E/S161E}$ mice. As anticipated (Berger et al., 2014), $Ripk1^{K45A/K45A}$ mice were resistant to lethal-dose TNF-induced death (Fig. 4 A). In contrast, $Ripk1^{K45A+S161E/K45A+S161E}$ mice were highly sensitive to TNF-induced death, similar to $Ripk1^{S161E/S161E}$ mice (Fig. 4 B). Similar results were obtained in $Ripk1^{S161E/S161E}$ mice when RIPK1 kinase inhibitors were used (Fig. 4 C). The ability of RIPK1 S161E mutant to transduce death signaling without the kinase activity suggests that a primary function of RIPK1's kinase activity in TNF-induced mouse death is to self-phosphorylate S161.

Consistently, BMDMs from $Ripk1^{K45A+S161E/K45A+S161E}$ mice underwent necroptosis in kinetics similar to that of BMDMs from $Ripk1^{S161E/S161E}$ mice when stimulated with TNF + zVAD, while $Ripk1^{K45A/K45A}$ BMDMs were completely resistant to TNF + zVAD stimulation (Fig. 4 D). In addition, S166 phosphorylation was readily detected in steady-state $Ripk1^{S161E/S161E}$ BMDMs and enhanced by TNF + zVAD treatment, while in contrast, it was completely abolished in cells carrying the K45A mutation, regardless of the treatment (Fig. 4 E). $Ripk1^{K45A+S161E/K45A+S161E}$ BMDMs underwent TNF + zVAD-induced necroptosis efficiently in the absence of detectable S166 phosphorylation (Fig. 4, D and E). Taken together, these *in vivo* and *in vitro* data (Figs. 3 and 4) (Zhang et al., 2017) demonstrate that S161 phosphorylation, which can bypass the defect of the kinase-dead mutation of RIPK1, is crucial for autophosphorylation of S166 and TNF-induced cell death.

IEC necroptosis triggers TNF-induced death of $Ripk1^{S161E/S161E}$ mice

To determine the contributions of hematopoietic and non-hematopoietic lineages in the death of $Ripk1^{S161E/S161E}$ mice, reciprocal bone marrow transplantation was conducted by transplanting WT or $Ripk1^{S161E/S161E}$ bone marrow into irradiated WT or $Ripk1^{S161E/S161E}$ recipient mice. It was observed that the bone marrow transplanted mice are generally more susceptible to death (He et al., 2024), so we adjusted the dose of TNF in this experiment. All mice carrying $Ripk1^{S161E/S161E}$ non-hematopoietic

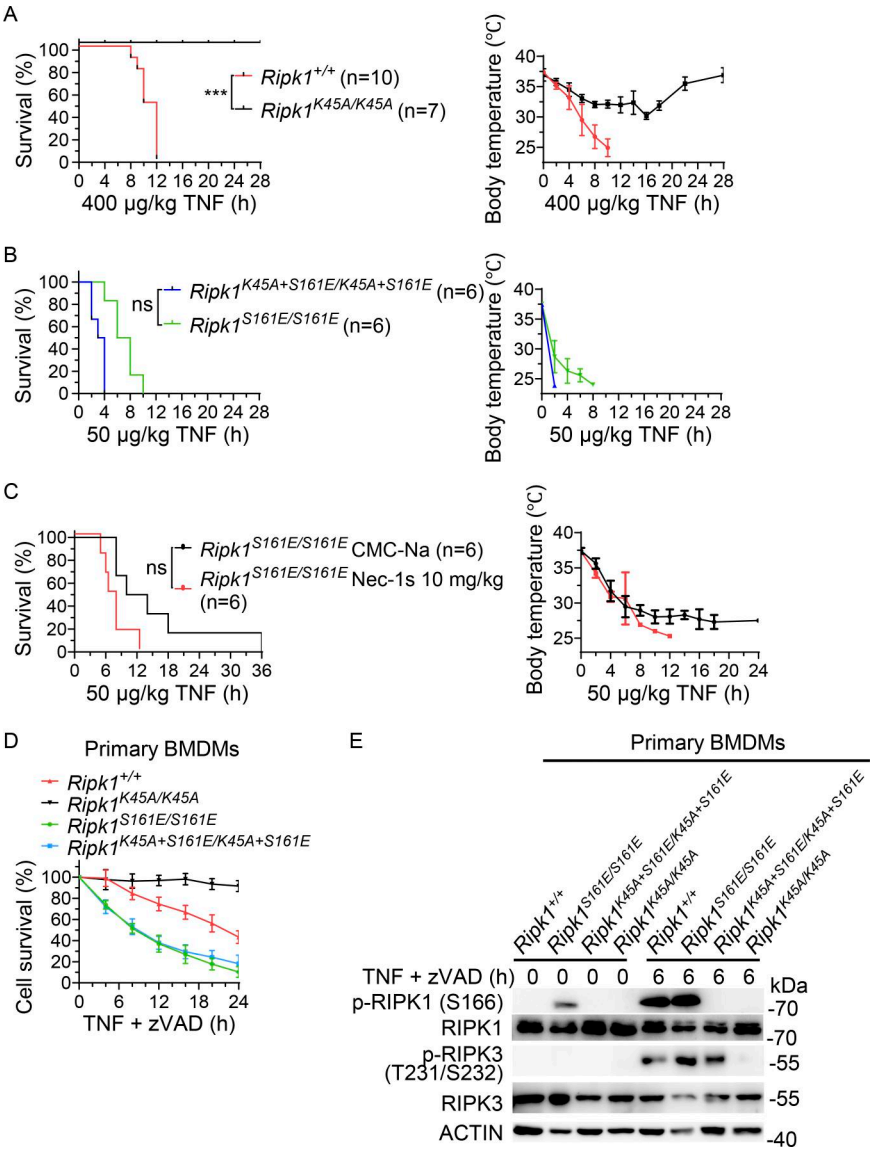

Figure 4. **Mimicking S161 phosphorylation can compensate for the loss of RIPK1 kinase activity in initiating TNF-induced mouse death. (A–C)** Survival curves and body temperature of 8- to 12-wk-old male littermate mice after TNF injection (400 μg/kg i.v. for *Ripk1*$^{+/+}$ and *Ripk1*$^{K45A/K45A}$ mice; 50 μg/kg i.v. for *Ripk1*$^{S161E/S161E}$ and *Ripk1*$^{K45A+S161E/K45A+S161E}$ mice). Before TNF injection in C, *Ripk1*$^{S161E/S161E}$ mice were intragastrically administered with Necrostatin 1S (Nec-1s) or sodium carboxymethyl cellulose (CMC-Na). Mouse survival is presented as a Kaplan–Meier plot, and the log-rank test is performed. ns, $P \geq 0.05$; ***$P < 0.001$. Data of body temperature are presented as mean ± SD. **(D)** Primary BMDMs from *Ripk1*$^{+/+}$, *Ripk1*$^{K45A/K45A}$, *Ripk1*$^{S161E/S161E}$, and *Ripk1*$^{K45A+S161E/K45A+S161E}$ mice were treated with TNF (10 ng/ml) + zVAD (20 μM) for the indicated time points. Survival of cells from three mice of each genotype was measured. All mice were 8- to 12-wk-old male littermates. Data are presented as mean ± SD. **(E)** Cell lysates of primary BMDMs of indicated genotypes treated with or without TNF (10 ng/ml) + zVAD (20 μM) for 6 h were analyzed by immunoblotting to detect proteins as indicated. The above experiments were independently performed twice. Source data are available for this figure: SourceData F4.

cells died rapidly upon 50 μg/kg of TNF treatment, regardless of the genotypes of the transplanted bone marrow. In contrast, only a portion of the WT recipients with *Ripk1*$^{S161E/S161E}$ hematopoietic cells died after TNF injection (Fig. 5 A). Reciprocal bone marrow transplantation using WT and *Ripk1*$^{S161N/S161N}$ mice showed that all *Ripk1*$^{S161N/S161N}$ recipients were similarly resistant to TNF, regardless of the genotype of the transplanted bone marrow. Conversely, all WT recipients were comparably sensitive to an adjusted lethal dose (200 μg/kg) of TNF, regardless of the genotype of the transplanted bone marrow (Fig. 5 B), indicating that mimicking RIPK1 S161 phosphorylation in non-hematopoietic cells enhances animal lethality. On the other hand, phosphorylation of S161 in hematopoietic cells may still contribute slightly to the death (Fig. 5 A). We also measured immune cell populations in WT and S161E mutant mice and did not detect significant differences (Fig. S4, A and B). It has been reported that the kinase-dead mutation of RIPK1 affects mainly non-hematopoietic cells (Zelic et al., 2018), and here we showed similarly that non-hematopoietic cells are the pivotal contributors to TNF-induced lethality in *Ripk1*$^{S161E/S161E}$ mice.

A number of *in vivo* studies have suggested that TNF-induced SIRS is associated with the massive death of IECs (Chen et al., 2015; Newton et al., 2016; Wu et al., 2024a). Given that the cecum in *Ripk1*$^{S161E/S161E}$ mice is the key effector organ (Fig. 1) and non-hematopoietic cells are the main contributors to TNF-induced animal death, we hypothesized that necroptosis of IECs in the cecum is the initial cause of death of TNF-challenged *Ripk1*$^{S161E/S161E}$ mice. To examine this possibility, *Ripk3* was conditionally ablated in *Ripk1*$^{S161E/S161E}$ IECs by generating the *Ripk1*$^{S161E/S161E}$ *Ripk3*$^{f/f}$ *Villin-cre*$^{+/-}$ mice (Fig. S4 C). As anticipated, *Ripk3* absence in the IECs prevented TNF-induced death of *Ripk1*$^{S161E/S161E}$ mice (Fig. 5 C), the release of LDH into the blood (Fig. 5 D), and cecal damage (Fig. 5 E). Consistently, immunofluorescence analysis revealed increased necroptosis in the IECs and in Ki-67^{+} crypt cells in TNF-treated *Ripk1*$^{S161E/S161E}$ ceca, which was completely abolished by the loss of intestinal epithelial *Ripk3*

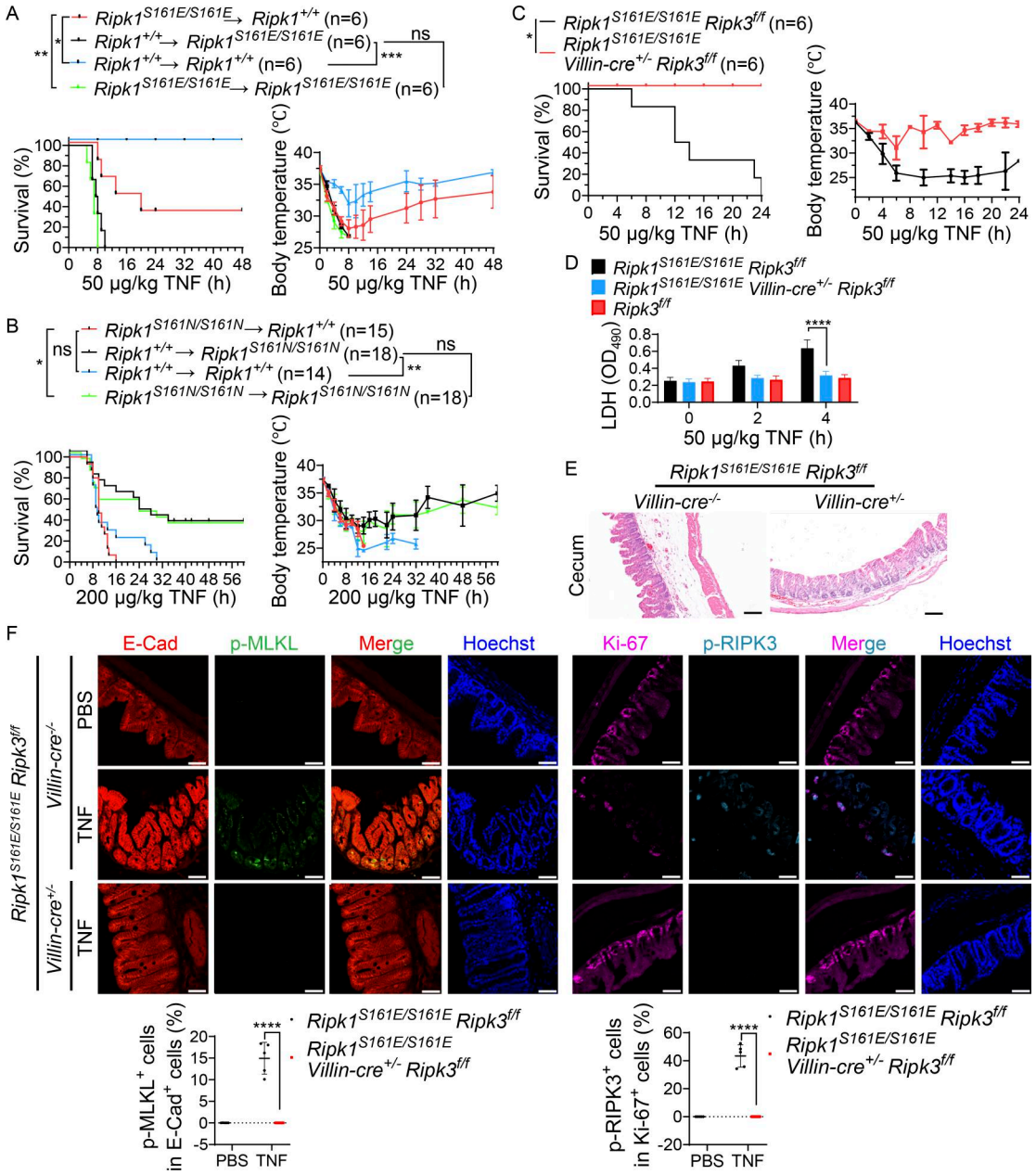

Figure 5. **IEC necroptosis triggers TNF-induced death of *Ripk1*$^{S161E/S161E}$ mice. (A and B)** Survival curves and body temperature of 14-wk-old male littermate bone marrow–transplanted *Ripk1*$^{+/+}$, *Ripk1*$^{S161E/S161E}$, or *Ripk1*$^{S161N/S161N}$ mice after injection with TNF (50 μg/kg i.v. in A, 200 μg/kg i.v. in B). Mouse survival is presented as a Kaplan–Meier plot, and the log-rank test is performed. ns, P ≥ 0.05; *P < 0.05; **P < 0.01; ***P < 0.001. Data of body temperature are presented as mean ± SD. **(C)** Survival curves and body temperature of 8- to 12-wk-old male littermate mice of the indicated genotypes after TNF injection (50 μg/kg, i.v.). **(D)** Mice (n = 6) of the indicated genotypes were i.v. injected with TNF (50 μg/kg). At the indicated time points, serum samples were collected for measurements of LDH release. Data are presented as mean ± SD. P values are determined by a two-tailed, unpaired t test. ****P < 0.0001. **(E)** Representative H&E staining images of ceca from three mice of each indicated genotype i.v. treated with 50 μg/kg of TNF for 6 h. Scale bars, 100 μm. **(F)** Representative immunofluorescence staining images of ceca from five mice of each indicated genotype after TNF treatment for 6 h (50 μg/kg, i.v.). E-cadherin (E-Cad, red), phospho-MLKL S345 (p-MLKL, green), Ki-67 (purple), phospho-RIPK3 T231 + S232 (p-RIPK3, light blue), and Hoechst (blue). Scale bars, 50 μm. Percentages of p-MLKL$^+$ cells in E-Cad$^+$ cells and p-RIPK3$^+$ cells in Ki-67$^+$ cells were quantified using ImageJ. Data are presented as mean ± SD. P values are determined by a two-tailed, unpaired t test. ****P < 0.0001. All mice were 8- to 12-wk-old male littermates (D–F). The above experiments were independently performed twice.

(Fig. 5 F). In contrast, no cleaved caspase-3 signals were observed in either WT or *Ripk1*$^{S161E/S161E}$ ceca after TNF injection (Fig. S4 D). Collectively, our data demonstrate that the necroptosis of IECs is essential in TNF-induced death of *Ripk1*$^{S161E/S161E}$ mice.

Cecal EC necroptosis is another trigger of TNF-induced death, and the necroptosis of ECs and IECs promotes each other reciprocally in the cecum of TNF-treated *Ripk1*$^{S161E/S161E}$ mice

It was reported that endothelial necroptosis underlies SIRS (Wu et al., 2024b; Zelic et al., 2018), and indeed, lethal-dose TNF

caused vascular leakage in the cecum in WT mice (Fig. S4 E). We examined the differences introduced by the S161E mutation and found that S161E enabled 50 μg/kg of TNF to increase vascular permeability in the cecum and lung, but not in other organs (Fig. 6 A). To determine whether endothelial necroptosis contributes to TNF-induced death of *Ripk1*$^{S161E/S161E}$ mice, *Ripk3* was deleted specifically in ECs by generating the *Ripk1*$^{S161E/S161E}$ *Ripk3*$^{f/f}$ *Tie2-cre*$^{+/-}$ mice and the tamoxifen-treated *Ripk1*$^{S161E/S161E}$ *Ripk3*$^{f/f}$ *Cdh5-ERT2-cre*$^{+/-}$ mice (Fig. S4 C). Remarkably, the loss of *Ripk3* in the ECs blocked vascular leakage in the cecum of *Ripk1*$^{S161E/S161E}$ mice (Fig. 6 B), similar to the effect of *Ripk3* deficiency on lethal-dose TNF-induced vascular leakage in the cecum of WT mice (Fig. S4 F). It should be noted that the increased vascular leakage in the lungs of *Ripk1*$^{S161E/S161E}$ mice is unrelated to RIPK3 signaling in ECs. We also measured LDH in the blood and monitored mouse survival and found that *Ripk3* KO in the ECs abolished TNF-induced serum LDH release (Fig. 6 C) and rescued the death of *Ripk1*$^{S161E/S161E}$ mice (Fig. 6, D and E), similar to what we had observed in IEC-specific *Ripk3* KO mice (Fig. 5, C and D). Interestingly, the deletion of *Ripk3* in the ECs not only prevented endothelial necroptosis (Fig. 6 F) but also prohibited cecal damage (Fig. 6 G) and cecal IEC death (Fig. 6 H). Encouraged by this observation, we further investigated whether IEC necroptosis has an impact on EC necroptosis. Astonishingly, the deletion of *Ripk3* in IECs conversely alleviated cecal vascular leakage (Fig. 6 I) and reduced EC necroptosis (Fig. 6 J). Thus, necroptosis of IECs and ECs in the cecum appears to promote each other reciprocally, forming a positive amplifying loop that results in TNF-induced cecal damage.

Necroptosis raises IL-6 levels in the circulation, which facilitates the death of *Ripk1*$^{S161E/S161E}$ mice

Cytokines play important roles in systemic inflammatory responses (Jaffer et al., 2010). Among all the tested pro-inflammatory cytokines and chemokines, IL-6 was the only one whose induction by 50 μg/kg of TNF was enhanced by the S161E mutation (Fig. 7 A and Fig. S5 A). And interestingly, serum IL-6 in 50 μg/kg of TNF-treated *Ripk1*$^{S161E/S161E}$ mice reached levels comparable with those in lethal-dose TNF-treated WT mice (Fig. 7 A). Due to the correlation between IL-6 induction and animal death, we examined the effect of *Il-6* deletion and found that genetic loss of *Il-6* greatly alleviated cecal edema but did not affect cecal damage (Fig. 7 B) nor necroptosis of IECs or ECs (Fig. S5 B). Ablation of *Il-6* restored cecal vascular integrity (Fig. 7 C and Fig. S5 C) and partially rescued animal death (Fig. 7 D) in TNF-treated *Ripk1*$^{S161E/S161E}$ mice. Thus, IL-6 promotes vascular leakage in TNF-induced SIRS.

To identify the producing cells of IL-6, real-time quantitative PCR analysis was conducted. TNF induced *Il-6* transcription in the cecum but not in other parts of the intestine (Fig. 7 E), and in the lung and spleen but not in other organs (Fig. S5 D) of *Ripk1*$^{S161E/S161E}$ mice. Bone marrow transplantation analysis revealed that as long as the recipient *Ripk1*$^{S161E/S161E}$ mice carried the *Il-6* gene, IL-6 can be detected in the serum upon TNF treatment regardless of the genotypes of the donor bone marrow (Fig. 7 F), indicating that serum IL-6 was produced by non-hematopoietic cells. Thus, TNF induces IL-6 production in non-hematopoietic cells in the cecum, lung, and spleen of *Ripk1*$^{S161E/S161E}$ mice.

Since deletion of *Ripk3* or *Mlkl* prevents the S161E mutation–caused sensitization of mice to TNF-induced death, we measured serum IL-6 in these mice. The loss of *Ripk3* or *Mlkl* prohibited IL-6 release into the serum (Fig. 7 G), indicating that the accumulation of IL-6 in the blood is a necroptosis-elicited event. Similar to the mutually promoting effect of IEC necroptosis and EC necroptosis shown in Fig. 6, either blocking the IEC necroptosis or preventing the EC necroptosis was sufficient to abolish serum IL-6 accumulation (Fig. 7 H). Collectively, our data indicated that the IL-6 accumulation in the blood of 50 μg/kg of TNF-treated *Ripk1*$^{S161E/S161E}$ mice originates from non-hematopoietic cells. The circulating IL-6 is elicited by necroptosis and accelerates cecal vascular leakage and the final death of *Ripk1*$^{S161E/S161E}$ mice.

Discussion

Phosphorylation is a key regulatory mechanism of RIPK1. Here we demonstrate that RIPK1 S161 autophosphorylation is crucial for TNF-induced cecal damage and subsequent mouse death. Furthermore, we uncovered that further autophosphorylation of RIPK1 is most likely initiated at S161, which cascades to S166 and possibly other sites subsequently. Mice with the phospho-mimic RIPK1 S161E mutation have enhanced sensitivity to TNF challenge, which allows us to study TNF-induced mouse death using low-dose TNF (50 μg/kg). As low-dose TNF stimulation should elicit less intense irrelevant responses (background noise) than high-dose TNF, *Ripk1*$^{S161E/S161E}$ mice enabled us to reveal that the necroptosis of IECs and ECs positively influences each other in the progression of TNF-induced cecal damage and that among the cytokines tested, only the IL-6 accumulation in the circulation of TNF-treated mice depends on the occurrence of necroptosis. Our *in vitro* and *in vivo* data showed that the autophosphorylation of S161 and subsequent phosphorylation in RIPK1 is the primary function of RIPK1 kinase activity in TNF-induced cell death and animal death.

S166 phosphorylation in RIPK1 has been explored using the S166A mutant mice (Laurien et al., 2020), which showed that the S166A mutation attenuates RIPK1-mediated cell death *ex vivo*. In this study, we revealed that S166N completely blocks TNF-induced necroptosis in L929 cells, and as previously reported, the S166A mutation attenuates TNF-induced necroptosis (Fig. S3 E). Although S166 phosphorylation is crucial for TNF-induced necroptosis, the phospho-mimic S166E mutation does not gain function in mediating necroptosis. Instead, it attenuates TNF-induced necroptosis in L929 cells (Fig. S3 E). An interpretation of this phenomenon is that the glutamic acid mutation does not mimic the S166 phosphorylation, or the S166 phosphorylation cannot drive further phosphorylation (Fig. S3 F), and therefore cannot execute necroptosis.

Unlike the S166E mutation, the phospho-mimic S161E leads to spontaneous S166 phosphorylation in primary *Ripk1*$^{S161E/S161E}$ cells, IECs in *Ripk1*$^{S161E/S161E}$ mice, and RIPK1 S161E-reconstituted L929 cells (Fig. 3, C–G and Fig. S3, B–D), and the S161E mutant is the only phospho-mimic mutant among the 37 tested ones that can bypass the effect of kinase blockade to mediate TNF-induced

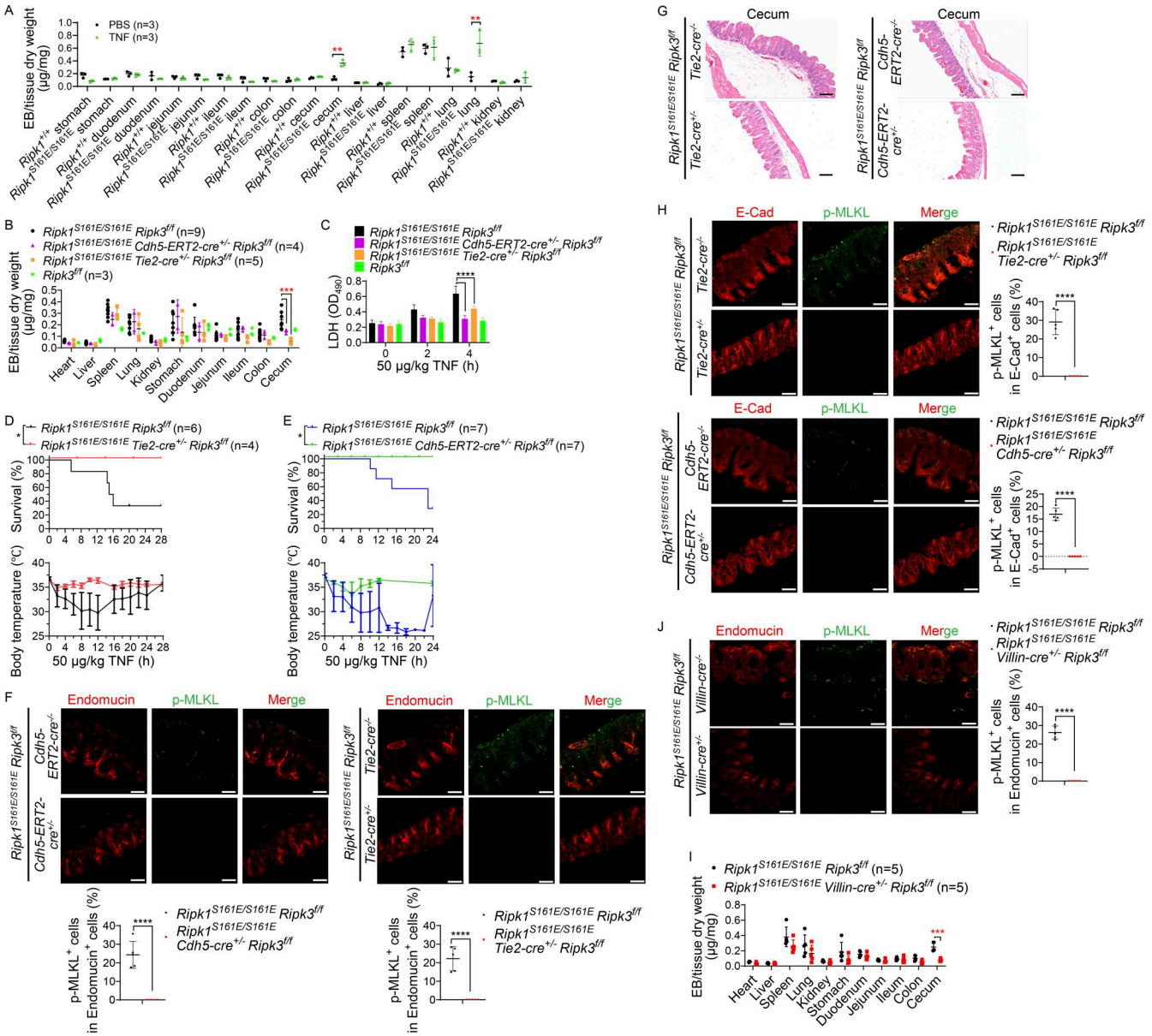

Figure 6. **Cecal EC necroptosis is another trigger of TNF-induced death, and the necroptosis of IECs and ECs in the cecum of TNF-treated *Ripk1*$^{S161E/S161E}$ mice promotes each other reciprocally. (A, B, and I)** 4 h after TNF treatment (50 µg/kg, i.v.), 8- to 12-wk-old male littermate mice of the indicated genotypes were injected with EB (0.5 mg/mouse). Organs were collected 20 min after EB injection, and the amount of EB extracted from the organs was measured by spectrophotometry. **(C)** 8- to 12-wk-old male littermate mice (n = 6) of the indicated genotypes were i.v. injected with TNF (50 µg/kg). At the indicated time points, serum samples were collected for measurements of LDH release. **(D and E)** Survival curves and body temperature of 8- to 12-wk-old male littermate mice of the indicated genotypes after TNF injection (50 µg/kg, i.v.). Mouse survival is presented as a Kaplan–Meier plot, and the log-rank test is performed. *P < 0.05. Data of body temperature are presented as mean ± SD. **(F, H, and J)** Representative immunofluorescence staining images of ceca from five mice of each indicated genotype 6 h after TNF injection (50 µg/kg, i.v.). Endomucin (red) and p-MLKL (green) in F and J; E-Cad (red) and p-MLKL (green) in H. Scale bars, 50 µm. Percentages of p-MLKL$^+$ cells in Endomucin$^+$ cells (F and J) or in E-Cad$^+$ cells (H) were quantified using ImageJ. Data are presented as mean ± SD. P values are determined by a two-tailed, unpaired t test. ****P < 0.0001. **(G)** Representative H&E staining images of ceca from three mice of each indicated genotype 6 h after i.v. injection with 50 µg/kg of TNF. Scale bars, 100 µm. All mice were 8- to 12-wk-old male littermates (F–H and J). All 8-wk-old male *Ripk1*$^{S161E/S161E}$ *Cdh5-ERT2-cre*$^{+/-}$ *Ripk3*$^{f/f}$ mice and the littermate *Ripk1*$^{S161E/S161E}$ *Ripk3*$^{f/f}$ mice in this work were orally administered with 100 mg/kg of tamoxifen for 5 consecutive days. After a 10- to 14-days break, TNF was applied. Data are presented as mean ± SD. P values are determined by a two-tailed, unpaired t test. **P < 0.01; ***P < 0.001; ****P < 0.0001. The above experiments were independently performed twice.

necroptosis in L929 cells (Zhang et al., 2017). Since S161 phosphorylation leads to S166 phosphorylation but not vice versa, and S161E mutation can promote necroptosis in the absence of S166 phosphorylation (Fig. 4), we conclude that a primary function of RIPK1 kinase activity in TNF signaling *in vitro* and *in vivo* is to autophosphorylate S161. A fundamental role of RIPK1 S161 phosphorylation in TNF-induced necroptosis was also observed in human HT-29 cells (Fig. S5 E).

Several reports have shown that IEC necroptosis is required for TNF-induced mouse death (Chen et al., 2015; Newton et al.,

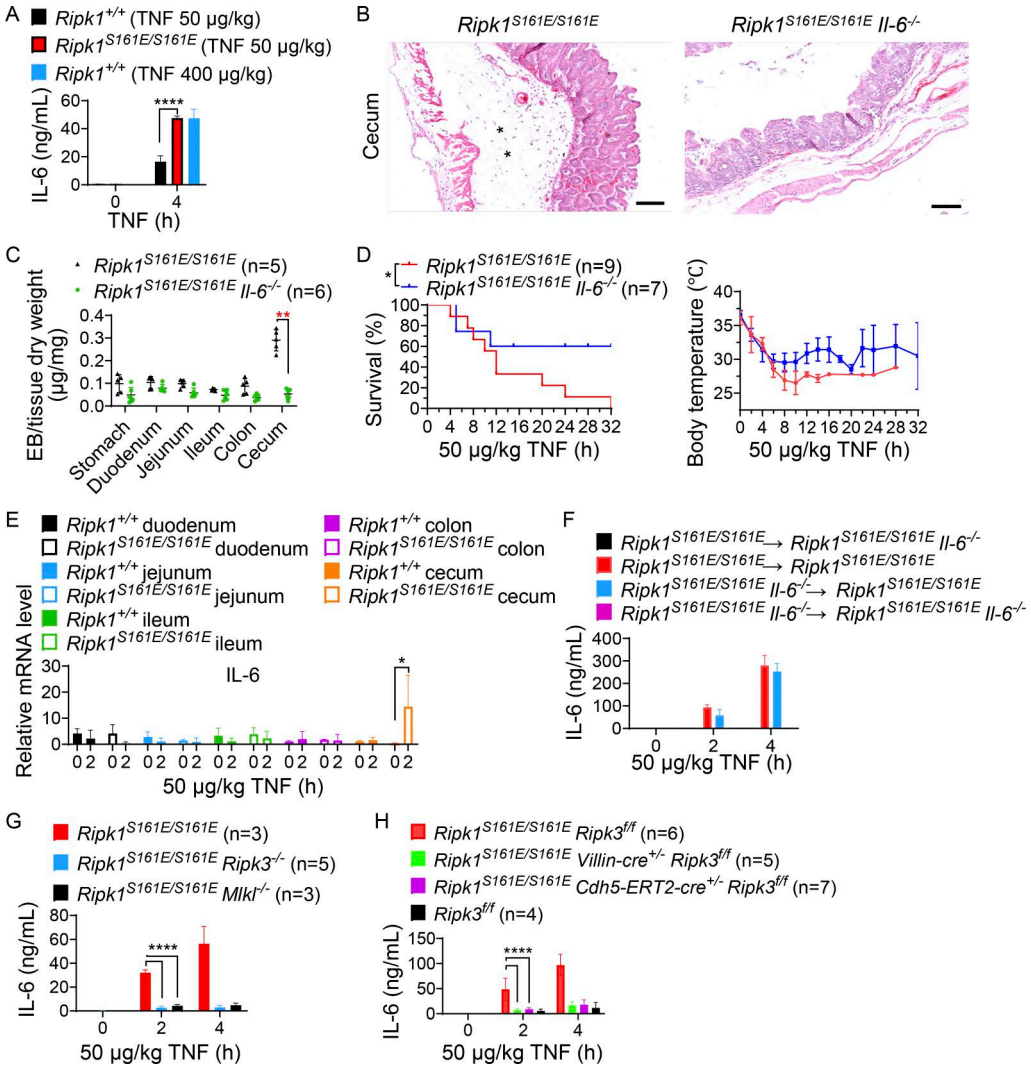

Figure 7. **Necroptosis raises IL-6 levels in the circulation, which facilitates the death of *Ripk1*$^{S161E/S161E}$ mice. (A)** Mice (n = 6) were i.v. injected with 50 μg/kg TNF or 400 μg/kg TNF as indicated. At the indicated time points, serum samples were collected for ELISA analysis of IL-6. All mice were 8- to 12-wk-old male littermates (A, B, and E). **(B)** Representative H&E staining images of ceca from three mice of each indicated genotype 6 h after i.v. injection with 50 μg/kg of TNF. Asterisks indicate areas of edema. Scale bars, 100 μm. **(C)** 8- to 12-wk-old male littermate mice of the indicated genotypes were treated with TNF (50 μg/kg, i.v.) for 4 h and then EB (0.5 mg/mouse) for 20 min. Organs were collected, and the amount of EB extracted from the organs was measured by spectrophotometry. **(D)** Survival curves and body temperature of 8- to 12-wk-old male littermate mice of the indicated genotypes after TNF injection (50 μg/kg, i.v.). Mouse survival is presented as a Kaplan–Meier plot, and the log-rank test is performed. *P < 0.05. Data of body temperature are presented as mean ± SD. **(E)** Quantitative RT-PCR analysis of *Il-6* mRNA levels in organs of *Ripk1*$^{+/+}$ and *Ripk1*$^{S161E/S161E}$ mice (n = 6) after TNF injection (50 μg/kg, i.v.) at the indicated time points. **(F)** 14-wk-old male littermate *Ripk1*$^{S161E/S161E}$ or *Ripk1*$^{S161E/S161E}$ *Il-6*$^{-/-}$ mice (n = 3) were reconstituted with *Ripk1*$^{S161E/S161E}$ or *Ripk1*$^{S161E/S161E}$ *Il-6*$^{-/-}$ bone marrow cells and then i.v. injected with TNF (50 μg/kg). At the indicated time points, serum samples were collected for ELISA analysis of IL-6. **(G and H)** 8- to 12-wk-old male littermate mice of the indicated genotypes were i.v. injected with TNF (50 μg/kg). At the indicated time points, serum samples were collected for ELISA analysis of IL-6. Data are presented as mean ± SD. P values are determined by a two-tailed, unpaired t test. *P < 0.05; **P < 0.01; ****P < 0.0001. The above experiments were independently performed twice.

2016; Wu et al., 2024a). RIPK1 S161E mutation sensitizes cecal epithelia to necroptosis (Fig. 5), supporting the idea that cecal epithelial cells are the most sensitive cells to TNF-induced necroptosis (Chen et al., 2015; Wu et al., 2024a). Involvement of endothelial necroptosis in TNF-induced SIRS has been reported (Wu et al., 2024b; Zelic et al., 2018) with evidence of the damaged liver vascular endothelium. Our data revealed that death-associated vascular leakage primarily occurs in the cecum (Fig. 6; and Fig. S4, E and F). It is possible that all vascular ECs are sensitive to TNF-induced necroptosis, but the sensitivity differs in different organs. Similar explanations may also apply to the IECs. We also observed an interesting phenomenon that necroptosis of the vascular ECs and IECs promotes each other in the cecum (Fig. 6). A possible interpretation is that the damaged endothelial barrier or the DAMPs released from necroptotic ECs promote/cause the death of IECs and vice versa.

Cytokine storms have long been viewed as an essential player in SIRS, but currently, no evidence shows that the cytokine or chemokine levels are good prognostic factors to predict survival of TNF-induced SIRS (Zelic et al., 2018). *Ripk1*$^{S161E/S161E}$ mice are

particularly sensitive to TNF-induced death, allowing us to identify IL-6 as a death contributor (Fig. 7). Furthermore, different from the common assumption, the elevation of IL-6 in the circulation is not a direct response to the injected TNF but is triggered by TNF-induced necroptosis (Fig. 7, G and H). The function of IL-6 is not to cause cell death but to exacerbate cecal edema and vascular permeability, shedding light on the role of IL-6 in TNF-induced SIRS.

In sum, this study demonstrated the role of RIPK1 S161 phosphorylation *in vivo* and revealed the relationship between S161 phosphorylation and S166 phosphorylation. Taking advantage of the *Ripk1*$^{S161E/S161E}$ mice that have enhanced necroptotic responses to TNF, we uncovered the linkage between necroptosis of the ECs and IECs in TNF-induced cecal damage and also found that the elevation of circulating IL-6 is a selective response to necroptosis. A co-submitted article also supports an important role of RIPK1 autophosphorylation at S161 in mediating cell death and inflammation (Koerner et al., 2025). A model of this pathogenesis is proposed in Fig. S5 F.

Materials and methods

Ethical statement

All mice were housed in specific pathogen–free conditions with a 12-h light/dark cycle and access to food and water *ad libitum* at Xiamen University Laboratory Animal Center. Animal husbandry and all mouse experiments were reviewed and approved by the Laboratory Animal Management and Ethics Committee of Xiamen University (approval number XMU-LAC20210072) and were in strict accordance with good animal practice as defined by Xiamen University Laboratory Animal Center.

Mice

Ripk1$^{S161E/S161E}$ mice, *Ripk1*$^{S161A/S161A}$ mice, *Ripk1*$^{S161N/S161N}$ mice, *Ripk1*$^{K45A/K45A}$ mice, *Ripk1*$^{K45A+S161E/K45A+S161E}$ mice, and *Ripk3*$^{f/f}$ mice were generated by Xiamen University Laboratory Animal Center as previously described (Gao et al., 2024; Zhang et al., 2021; Zhong et al., 2015). gRNA targeting sequence was 5′-CCA GATAGCCGATCTTGGTGTGG-3′ for *Ripk1* S161E, S161A, and S161N mutation; 5′-ATCCTGAAAAAAGTATACACAGG-3′ for *Ripk1* K45A mutation; and 5′-AAGTCAGCCTGGGTCCGTGAGGG-3′ and 5′-TATCAATAAAGGAACTGTGGGGG-3′ for loxp insertion into *Ripk3*. The loxp sequence was inserted into introns 3 and 9 of *Ripk3*, respectively, and by reacting with the Cre recombinase exons 4–9 were knocked out from *Ripk3*. *Casp8*$^{-/-}$ mice, *Ripk3*$^{-/-}$ mice, and *Mlkl*$^{-/-}$ mice were generated as described previously (Zhang et al., 2021). *Tie2-cre* mice and *Cdh5-ERT2-cre* mice were gifts from Prof. Xiao Yang (Academy of Military Sciences, Beijing, China) and Prof. Ralf H. Adams (Cancer Research UK London Research Institute, London, UK), respectively (Li et al., 2005; Wang et al., 2010). *Villin-cre* mice and *Il-6*$^{-/-}$ mice were from the Jackson Laboratory (stock #021504 and #002650; JAX). All mice generated in-house were on a C57BL/6 background. All KO/knock-in alleles of mice introduced from other institutes have been crossed onto the C57BL/6 background for at least six generations, and mice with H19 and DMR mutations were excluded by using PCR as previously reported (Zhong et al., 2015). All experiments in this study employed littermate controls to ensure genetic background consistency. Additional information is provided upon request.

Antibodies

Antibodies for immunofluorescence staining: cleaved caspase-3 (9661S; Cell Signaling Technology/CST), phospho-RIPK3 (2D7) (T231, S232) (ab205421; Abcam), phospho-MLKL (S345) (ab196436; Abcam), E-cadherin (14472S; CST), Ki-67 (12202S; CST), endomucin (sc-65495; Santa Cruz Biotechnology), Alexa Fluor 488 goat anti-mouse antibody (A11029; Invitrogen), Alexa Fluor 568 goat anti-mouse antibody (A11004; Invitrogen), Alexa Fluor 647 goat anti-rat antibody (A21247; Invitrogen), Alexa Fluor 488 goat anti-rabbit antibody (A11034; Invitrogen), and Alexa Fluor 568 goat anti-rabbit antibody (A11036; Invitrogen).

Antibodies for western blot: RIPK1 (3493S; CST), phospho-RIPK1 (S166) (31122S; CST), FADD (homemade), RIPK3 (homemade), phospho-RIPK3 (91702S; CST), MLKL (homemade), phospho-MLKL (S345) (ab196436; Abcam), caspase-3 (9662S; CST), cleaved caspase-3 (9661S; CST), E-cadherin (14472S; CST), endomucin (sc-65495; Santa Cruz Biotechnology), and ACTIN (T0022; Affinity).

Antibodies for flow cytometry: PerCP/Cy5.5 anti-CD45.2 (109828; BioLegend), PE/Cy7 anti-CD3ε (100320; BioLegend), APC/Cy7 anti-B220 (103224; BioLegend), FITC anti-CD19 (11-0193-82; eBioscience), Pacific Blue anti-CD4 (100534; BioLegend), APC anti-CD8a (100712; BioLegend), FITC anti-CD11b (101206; BioLegend), PE anti-F4/80 (123110; BioLegend), APC anti–Ly-6G (127614; BioLegend), APC/Cy7 anti–Ly-6C (128026; BioLegend), PE anti-CD11c (557401; BD Pharmingen), APC anti–MHC-II (17-5320-82; eBioscience), FITC anti-NK1.1 (108706; BioLegend), and PE/Cy7 anti-CD31 (102417; BioLegend).

Antibody for cell treatment: Rabbit anti–TNF-α antibody (A0277; ABclonal Biotechnology).

Key reagents

Recombinant murine TNF-α (315-01A; Peprotech), human TNF-α recombinant protein (PHC3011; Thermo Fisher Scientific), pan caspase inhibitor Z-VAD-FMK (FMK001; R&D), Emricasan (HY-10396; MCE), SMAC LCL161 (HY-15518; MCE), CHX (HY-12320; MCE), Necrostatin 1S (S8641; Selleckchem), sodium carboxymethyl cellulose (HY-Y0703; MCE), Evans blue (EB) (E2129; Sigma-Aldrich), tamoxifen (HY-13757A; MCE), and corn oil (C8267; Sigma-Aldrich).

Cell culture

Murine fibroblast cell line L929, colorectal carcinoma cell line CT26, and HT-29 cells were obtained from the American Type Culture Collection. All MEFs were harvested from embryos of embryonic day E10.5–E13.5. All cells were cultured in DMEM (Life Technologies) supplemented with 10% (vol/vol) FBS (Life Technologies), 1% (vol/vol) MEM nonessential amino acids solution (Life Technologies), and 100 U/ml penicillin/streptomycin (Sangon). BMDMs were generated by differentiating bone marrow progenitors from the tibia and femur for 7 days in DMEM supplemented with 10% (vol/vol) FBS and 30% (vol/vol)

L929-conditioned media. All cells were grown at 37°C in a humidified incubator containing 5% CO_2. All cell lines were well established and frequently checked by monitoring morphology and functionalities. All the cell lines were authenticated by STR analysis and were routinely tested to be mycoplasma free.

Cell death analysis

Cell death was analyzed using the CellTiter-Glo luminescent cell viability assay kit (G7571; Promega). The assay was performed according to the manufacturer's instructions. In brief, 10,000 cells were seeded in 96-well plates with white walls. After treatment, an equal volume of the CellTiter-Glo reagent was added to the cell culture medium, which had been equilibrated to room temperature for 15 min. Cells were shaken for 15 min. Luminescent recording was performed with a TECAN Spark multimode microplate reader (Tecan).

Cecal EC isolation

Prior to cecum isolation, mice were sacrificed and underwent whole-body blood replacement with saline perfusion. Ceca were then collected, washed twice with cold PBS to remove the contents, cut into pieces, and digested in 4 mg/ml of collagenase I solution, shaking at 220 rpm, 37°C for 1 h. The digestion was ended by using DMEM media containing 10% FBS. Ceca were ground on a 70-µm strainer sitting on a 50-ml conical tube. Filtered cells were collected, centrifuged at 650 *g* for 5 min, and the supernatant was discarded. PE/Cy7 anti-CD31 (1:100 diluted in PBS containing 2% FBS) was used to stain the cells for 30 min at 4°C, and cells were then washed three times using the FACS buffer (PBS containing 2% FBS). $CD31^+$ live cells were sorted out using flow cytometry. Roughly 3–4 × 10^4 cells obtained per mouse were seeded in one well of a 24-well plate pre-coated with 1% gelatin. DMEM media containing 20% FBS was used for the cell culture and was changed 6–8 h after seeding. Cells would reach 100% confluency 4–7 days after seeding and were dissociated from the plate and lysed in SDS sample buffer for western blot analysis.

Cecal IEC isolation

Mice were sacrificed. Ceca were collected, washed twice with cold PBS to remove the contents, and digested in 5–10 ml of cold 5 mM EDTA for 30 min on a rotor at 4°C. Discard the tissue. Cells were filtered through a 70-µm strainer sitting on a 50-ml conical tube, centrifuged at 500 *g* for 5 min at 4°C, and washed with PBS twice. Pellets were lysed in SDS sample buffer for western blot analysis.

TNF-induced SIRS in mice

8- to 12-wk-old male mice of the indicated genotypes (average weight 25 g) were injected i.v. with 10, 25, 50, 150, 200, 250, 400, 600, or 1,600 µg/kg mouse TNF diluted in endotoxin-free PBS. To delete *Ripk3* in $Ripk1^{S161E/S161E}$ *Cdh5-ERT2-cre*$^{+/-}$ $Ripk3^{f/f}$ mice, 8-wk-old male $Ripk1^{S161E/S161E}$ *Cdh5-ERT2-cre*$^{+/-}$ $Ripk3^{f/f}$ mice and their littermate $Ripk1^{S161E/S161E}$ $Ripk3^{f/f}$ mice were both orally administered with 100 mg/kg of tamoxifen for 5 consecutive days. After a 10- to 14-days break, TNF was injected. Animals were under intensive observation, and survival was checked every 30 min. Body temperature measured by rectal thermometry was recorded every 2 h with an electric thermometer (ALC-ET03; ALC Bio). Mice were sacrificed at the indicated time points or when body temperature was below 23.6°C (Newton et al., 2016). To prepare the 20 mg/ml stock solution of tamoxifen, corn oil was added to 200 mg of tamoxifen to bring the final volume to 10 ml. Ultrasonic was needed to facilitate the dissolution.

Bone marrow transplantation

6-wk-old recipient mice were irradiated using an irradiator (RS 2000 Pro; Rad Source Technologies) at a dose of 8 Gray. Bone marrow cells were isolated from femurs, tibias, and humeri of the donor mice, and erythrocytes were lysed by ACK lysis buffer (C3702; Beyotime). Bone marrow cells were i.v. injected into each recipient mouse 4–6 h after irradiation. The chimerism of the recipient mice was examined 4 wk later by PCR analysis of the genomic DNA extracted from the tail and the blood from the retro-orbital sinus for genotyping non-hematopoietic cells and hematopoietic cells, respectively.

Cecectomy

Cecectomy was performed as previously described (Voravuthikunchai and Lee, 1987). Briefly, 6- to 8-wk-old mice were anaesthetized, shaved off the belly fur, and then placed in a supine position on the operating table. An incision of 1.5–2 cm was made along the lower abdomen. The cecum was lifted out and ligated as close as possible to the ileocecal junction and then was cut near the ligation and removed. The intestine was always kept moist with gauze soaked in physiological saline until it was replaced into the abdominal cavity. Lastly, the abdomen was closed in layers. For the sham-operated mice, the ceca were lifted out, left outside the abdominal cavities for the same duration as with the cecectomized animals, tucked back into the animals, and then the abdomens were closed.

In vivo blood vessel permeability assay

4 h after the tail vein injection of mouse TNF, 8- to 12-wk-old male mice were injected i.v. with 100 µl EB solution (5 µg/µl) diluted in sterile PBS. After 15–20 min, the mice were anesthetized and subjected to heart perfusion. The heart, liver, spleen, lung, kidney, stomach, duodenum, jejunum, ileum, colon, and cecum were collected and put in 1.5-ml tubes. Tissues should be air-dried to eliminate the water content variability between different organs. Weigh the dry tissues and add 500 µl of formamide to each tissue sample. Transfer all tubes to a 55°C water bath or heat block, and incubate for 24–48 h to extract EB from the tissues. Centrifuge the formamide/EB mixture to pellet any remaining tissue fragments, and measure absorbance at 610 nm by using formamide as a blank. Finally, calculate µg EB extracted per mg tissue.

H&E staining and immunofluorescence

After animals were euthanized, the liver, spleen, kidney, lung, and cecum were collected immediately and fixed in 4% paraformaldehyde (PFA) in PBS for 24 h at room temperature. The duodenum, jejunum, ileum, and colon were flushed with ice-

cold PBS, coiled into a "Swiss roll," and fixed in 4% PFA in PBS for 24 h. The fixed tissues were dehydrated in ethanol, cleared in xylene, and embedded in paraffin blocks. 5-µm sections were cut, mounted on adhesion microscope slides (ZSGB-BIO), and stained with H&E. Representative images were captured and processed using identical settings on a Leica Aperio Versa 200 (Leica Camera AG) at Xiamen University.

For immunofluorescence staining of the cecum, paraffin sections were dewaxed, rehydrated, subjected to heat-induced antigen retrieval with Tris-citrate buffer, blocked in 1% BSA, and then incubated overnight at 4°C with rabbit anti-cleaved caspase-3, mouse anti–phospho-RIPK3 (2D7), or rabbit anti–phospho-MLKL (S345) along with mouse anti–E-cadherin, rabbit anti–Ki-67, or rat anti-endomucin, diluted in the blocking buffer. Cecal sections were washed three times with 0.02% PBS–Tween-20 and then incubated for 1 h at room temperature with fluorescent antibodies. Hoechst 33342 (C1022; Beyotime Biotechnology) was used as a nuclear (DNA) counterstain. Images were acquired on a Zeiss LSM 900 laser scanning confocal microscope (Carl Zeiss Microscopy GmbH).

LDH assay

Serum LDH release was measured using the Cytotoxicity LDH assay kit-WST (CK12-2000; Dojindo Molecular Technologies) following the manufacturer's instructions.

ELISA

Sera from mice were assayed for mouse IL-1β (88-7013A-77; Thermo Fisher Scientific), IL-6 (88-7064-77; Thermo Fisher Scientific), IFN-γ (88-7314-88; Thermo Fisher Scientific), CCL2 (88-7391-88; Thermo Fisher Scientific), and IL-12/13 p40 (88-7120-88; Thermo Fisher Scientific) according to the manufacturer's instructions.

Quantitative real-time PCR

Total RNA was extracted using RNAIso Plus reagent (9109; TAKARA) as previously described (Liu et al., 2023). In brief, 5 µg of total RNA was reverse-transcribed using oligo (dT) primer (5′-TTTTTTTTTTTTTTTTTTTT-3′) and M-MLV reverse transcriptase (BGI) to generate cDNA. The expression levels of IL-6 and GAPDH were measured by real-time PCR using Hieff qPCR SYBR Green Master Mix (11201ES08; Yeasen) on a CFX96 Real-time RT-PCR detection system (Bio-Rad). Primer sequences used in this study are listed as follows: *Il-6*: forward, 5′-CTGCAAGAGACTTCCATCCAG-3′, reverse, 5′-AGTGGTATAGACAGGTCTGTTGG-3′; *Gapdh*: forward, 5′-TGTGTCCGTCGTGGATCTGA-3′, reverse, 5′-CCTGCTTCACCACCTTCTTGA-3′. PCR was carried out for 35 cycles using the following program: denaturation at 95°C for 20 s, annealing at 58°C for 20 s, and elongation at 72°C for 20 s. *Gapdh* was used as the internal reference gene, and the target and reference genes had similar amplification efficiencies. Expression of the target gene was normalized to that of *Gapdh* to compensate for any difference in the concentration of samples in every run of qPCR. The threshold cycle ($2^{-\Delta\Delta Ct}$) method was used, and the fold change of the target gene in each sample relative to the biological control sample was plotted.

Flow cytometry

For cell surface marker staining, cells were incubated with antibodies in 1× FACS buffer (1% FBS in PBS) for 30 min at 4°C and washed with 1× FACS buffer twice before analysis. All the stained samples were kept at 4°C. Flow cytometry data were acquired using a Fortessa X-20 flow cytometer (B&D) and analyzed with the FlowJo software (version 10.6.2).

Immunoblotting

Cells were harvested at the indicated time points, washed with PBS, lysed with 2× SDS sample buffer containing 100 mM dithiothreitol, and boiled at 100°C for 10 min. The samples were subjected to SDS-PAGE (PowerPac Basic and PowerPac Universal Power Supply; Bio-Rad), and images were acquired using an Image Quant LAS 4000 mini biomolecular imager (General Electric Company).

Immunoprecipitation

Cells were pelleted in ice-cold PBS and resuspended in lysis buffer (12.5 mM HEPES [pH 7.5], 30 mM NaCl, 90 mM NaSCN, 1% NP40, and protease inhibitor cocktail). Cells were lysed at 4°C for 30 min and then were sonicated and centrifuged at 20,000 × *g* for 30 min at 4°C. The supernatants were immunoprecipitated with Anti-FLAG M2 beads (A2220; Sigma-Aldrich) overnight at 4°C. Samples were washed three times in lysis buffer and then were eluted in 60 µl 2× SDS by shaking. The total cell lysates and immunoprecipitated samples were then subjected to SDS-PAGE.

MS

To determine the phosphorylation sites by MS, Flag-RIPK1 was immunoprecipitated with M2 beads from untreated *Ripk1* KO L929 cells expressing Flag-RIPK1 WT or Flag-RIPK1 S161E. Proteins in immunoprecipitated samples were analyzed by quantitative MS as previously described (Zhang et al., 2017) using MS TripleTOF 5600. MS data analyses were performed with PeakView (version 2.2) software.

Confocal microscopy

For immunostaining, cells were grown on coverslips (801008; NEST) coated with poly-L-lysine (P1399; Sigma-Aldrich). Cells were fixed with freshly prepared 3.7% formaldehyde for 15 min at room temperature and then permeabilized with 0.2% Triton X-100 in PBS. After being blocked with 3% BSA for 30 min, the samples were stained with primary antibodies at 4°C overnight, washed three times with PBS, and incubated with secondary antibodies for 1 h at room temperature. The slides were mounted with antifade reagent (P36934; Invitrogen) and imaged on a Zeiss LSM 900 laser scanning confocal microscope (Carl Zeiss Microscopy GmbH).

STORM imaging

STORM imaging was performed on an N-STORM microscope (Ti-E; Nikon Instruments) as previously described (Chen et al., 2022). Briefly, the N-STORM system uses an Agilent MLC-400B laser launch with a red diode laser (647 nm, 300 mW; MPBC), a green solid-state laser (561 nm, 150 mW; Coherent), a blue solid-state laser (488 nm, 200 mW; Coherent), a violet diode laser (405

nm, 100 mW; Coherent), and a 100× NA 1.49 oil immersion objective. STORM images were analyzed and molecularly modeled. PyMOL (The PyMOL Molecular Graphics System, Version 2.4 Schrödinger) was used to generate all the figures.

Statistical analysis

Statistical analysis was performed with GraphPad Prism software. Data were presented as mean ± SD of triplicate. Two-tailed Student's *t* test was used to compare differences between the two groups. Mouse survival was presented as a Kaplan–Meier plot and compared by the log-rank (Mantel–Cox) test. Differences in compared groups were considered statistically significant with P values. ns, P ≥ 0.05; *P < 0.05; **P < 0.01; ***P < 0.001; ****P < 0.0001. No statistical method was used to predetermine the sample size. No data were excluded from the analyses.

Online supplemental material

Fig. S1 presents the influence of RIPK1 S161E mutation on mouse development and organ/cell sensitivity to TNF (related to Fig. 1). Fig. S2 shows the function of RIPK1 S161 phosphorylation on apoptosis in CT26 cells and in primary BMDMs (related to Fig. 2). Fig. S3 displays the impact of RIPK1 S161E on RIPK3 recruitment to the necrosome, RIPK1 S166 phosphorylation, and cell death; it also shows data on RIPK1 S166 mutations affecting cell death and other phosphorylation events in RIPK1 (related to Fig. 3). Fig. S4 shows that the TNF-induced death of *Ripk1*$^{S161E/S161E}$ mice is not mainly caused by changes in hematopoietic cells or the apoptotic signaling but is a result of necroptosis of cecal IECs and ECs (related to Figs. 5 and 6). Fig. S5 exhibits data showing the role of IL-6 in TNF-induced death of *Ripk1*$^{S161E/S161E}$ mice (related to Fig. 7).

Data availability

Data are available in the published article and its online supplemental material.

Acknowledgments

We thank Lu Zhou (Xiamen University) for proofreading and editing the manuscript.

This work was supported by the National Key R&D Program of China (2020YFA0803500 to Jiahuai Han), the National Natural Science Foundation of China (grant 82388201 to Jiahuai Han; grant 31801158 to Yingying Zhang), the Chinese Academy of Medical Sciences Innovation Fund for Medical Sciences (2019-I2M-5-062 to Jiahuai Han), the Fujian Province Central to Local Science and Technology Development Special Program (2022L3079 to Jiahuai Han), and the FuXia-Quan Zi-Chuang District Cooperation Program (3502ZCQXT2022003 to Jiahuai Han). The funders had no role in study design, data collection and analysis, decision to publish, or manuscript preparation.

Author contributions: Tao Han: data curation, formal analysis, investigation, methodology, software, and validation. Chenchen Ruan: investigation, methodology, and validation. Huiyong Lin: investigation, methodology, and validation. Yuxia Zhang: investigation, methodology, and validation. Lang Li: investigation, methodology, and validation. Ye-hsuan Sun: investigation, methodology, and validation. Chuan-Qi Zhong: methodology. Xin Chen: investigation, methodology, validation, and visualization. Kai Huang: investigation, methodology, and validation. Yating Cao: validation. Zusen Fan: formal analysis and funding acquisition. Hongbing Zhang: resources. Jiahuai Han: conceptualization, formal analysis, funding acquisition, methodology, project administration, resources, supervision, and writing—original draft, review, and editing. Yingying Zhang: conceptualization, formal analysis, funding acquisition, investigation, methodology, project administration, resources, supervision, validation, and writing—original draft, review, and editing.

Disclosures: The authors declare no competing interests exist.

Submitted: 7 February 2025
Revised: 1 June 2025
Accepted: 15 July 2025

References

Annibaldi, A., S. Wicky John, T. Vanden Berghe, K.N. Swatek, J. Ruan, G. Liccardi, K. Bianchi, P.R. Elliott, S.M. Choi, S. Van Coillie, et al. 2018. Ubiquitin-mediated regulation of RIPK1 kinase activity independent of IKK and MK2. *Mol. Cell.* 69:566–580.e5. https://doi.org/10.1016/j.molcel.2018.01.027

Berger, S.B., V. Kasparcova, S. Hoffman, B. Swift, L. Dare, M. Schaeffer, C. Capriotti, M. Cook, J. Finger, A. Hughes-Earle, et al. 2014. Cutting edge: RIP1 kinase activity is dispensable for normal development but is a key regulator of inflammation in SHARPIN-deficient mice. *J. Immunol.* 192: 5476–5480. https://doi.org/10.4049/jimmunol.1400499

Chakraborty, R.K., and B. Burns. 2024. Systemic inflammatory response syndrome. *In* StatPearls. Copyright © 2024, StatPearls Publishing LLC., Treasure Island (FL).

Chan, F.K.-M., K. Moriwaki, and M.J. De Rosa. 2013. Detection of necrosis by release of lactate dehydrogenase activity. *Methods Mol. Biol.* 979:65–70. https://doi.org/10.1007/978-1-62703-290-2_7

Chen, W., J. Wu, L. Li, Z. Zhang, J. Ren, Y. Liang, F. Chen, C. Yang, Z. Zhou, S.S. Su, et al. 2015. Ppm1b negatively regulates necroptosis through dephosphorylating Rip3. *Nat. Cell Biol.* 17:434–444. https://doi.org/10.1038/ncb3120

Chen, X., R. Zhu, J. Zhong, Y. Ying, W. Wang, Y. Cao, H. Cai, X. Li, J. Shuai, and J. Han. 2022. Mosaic composition of RIP1-RIP3 signalling hub and its role in regulating cell death. *Nat. Cell Biol.* 24:471–482. https://doi.org/10.1038/s41556-022-00854-7

Cho, Y.S., S. Challa, D. Moquin, R. Genga, T.D. Ray, M. Guildford, and F.K.-M. Chan. 2009. Phosphorylation-driven assembly of the RIP1-RIP3 complex regulates programmed necrosis and virus-induced inflammation. *Cell.* 137:1112–1123. https://doi.org/10.1016/j.cell.2009.05.037

De Cesaris, P., D. Starace, A. Riccioli, F. Padula, A. Filippini, and E. Ziparo. 1998. Tumor necrosis factor-alpha induces interleukin-6 production and integrin ligand expression by distinct transduction pathways. *J. Biol. Chem.* 273:7566–7571. https://doi.org/10.1074/jbc.273.13.7566

Degterev, A., J. Hitomi, M. Germscheid, I.L. Ch'en, O. Korkina, X. Teng, D. Abbott, G.D. Cuny, C. Yuan, G. Wagner, et al. 2008. Identification of RIP1 kinase as a specific cellular target of necrostatins. *Nat. Chem. Biol.* 4: 313–321. https://doi.org/10.1038/nchembio.83

Dondelinger, Y., M.A. Aguileta, V. Goossens, C. Dubuisson, S. Grootjans, E. Dejardin, P. Vandenabeele, and M.J.M. Bertrand. 2013. RIPK3 contributes to TNFR1-mediated RIPK1 kinase-dependent apoptosis in conditions of cIAP1/2 depletion or TAK1 kinase inhibition. *Cell Death Differ.* 20:1381–1392. https://doi.org/10.1038/cdd.2013.94

Dondelinger, Y., T. Delanghe, D. Priem, M.A. Wynosky-Dolfi, D. Sorobetea, D. Rojas-Rivera, P. Giansanti, R. Roelandt, J. Gropengiesser, K. Ruckdeschel, et al. 2019. Serine 25 phosphorylation inhibits RIPK1 kinase-dependent cell death in models of infection and inflammation. *Nat. Commun.* 10:1729. https://doi.org/10.1038/s41467-019-09690-0

Dondelinger, Y., T. Delanghe, D. Rojas-Rivera, D. Priem, T. Delvaeye, I. Bruggeman, F. Van Herreweghe, P. Vandenabeele, and M.J.M. Bertrand. 2017. MK2 phosphorylation of RIPK1 regulates TNF-mediated cell death. *Nat. Cell Biol.* 19:1237–1247. https://doi.org/10.1038/ncb3608

Dondelinger, Y., S. Jouan-Lanhouet, T. Divert, E. Theatre, J. Bertin, P.J. Gough, P. Giansanti, A.J.R. Heck, E. Dejardin, P. Vandenabeele, and M.J.M. Bertrand. 2015. NF-κB-Independent role of IKKα/IKKβ in preventing RIPK1 kinase-dependent apoptotic and necroptotic cell death during TNF signaling. *Mol. Cell.* 60:63–76. https://doi.org/10.1016/j.molcel.2015.07.032

Duprez, L., N. Takahashi, F. Van Hauwermeiren, B. Vandendriessche, V. Goossens, T. Vanden Berghe, W. Declercq, C. Libert, A. Cauwels, and P. Vandenabeele. 2011. RIP kinase-dependent necrosis drives lethal systemic inflammatory response syndrome. *Immunity*. 35:908–918. https://doi.org/10.1016/j.immuni.2011.09.020

Gao, X., T. Teng, Y. Liu, T. Ai, R. Zhao, Y. Fu, P. Zhang, J. Han, and Y. Zhang. 2024. Anthrax lethal toxin and tumor necrosis factor-α synergize on intestinal epithelia to induce mouse death. *Protein Cell*. 15:135–148. https://doi.org/10.1093/procel/pwad050

Grimsrud, P.A., J.J. Carson, A.S. Hebert, S.L. Hubler, N.M. Niemi, D.J. Bailey, A. Jochem, D.S. Stapleton, M.P. Keller, M.S. Westphall, et al. 2012. A quantitative map of the liver mitochondrial phosphoproteome reveals posttranslational control of ketogenesis. *Cell Metab.* 16:672–683. https://doi.org/10.1016/j.cmet.2012.10.004

Günther, C., E. Martini, N. Wittkopf, K. Amann, B. Weigmann, H. Neumann, M.J. Waldner, S.M. Hedrick, S. Tenzer, M.F. Neurath, and C. Becker. 2011. Caspase-8 regulates TNF-α-induced epithelial necroptosis and terminal ileitis. *Nature*. 477:335–339. https://doi.org/10.1038/nature10400

He, P., T. Ai, M. Qiao, Z.-H. Yang, and J. Han. 2024. Phosphorylation of caspase-8 by RSKs via organ-constrained effects controls the sensitivity to TNF-induced death. *Cell Death Discov.* 10:255. https://doi.org/10.1038/s41420-024-02024-0

He, S., L. Wang, L. Miao, T. Wang, F. Du, L. Zhao, and X. Wang. 2009. Receptor interacting protein kinase-3 determines cellular necrotic response to TNF-alpha. *Cell*. 137:1100–1111. https://doi.org/10.1016/j.cell.2009.05.021

Holler, N., R. Zaru, O. Micheau, M. Thome, A. Attinger, S. Valitutti, J.L. Bodmer, P. Schneider, B. Seed, and J. Tschopp. 2000. Fas triggers an alternative, caspase-8-independent cell death pathway using the kinase RIP as effector molecule. *Nat. Immunol.* 1:489–495. https://doi.org/10.1038/82732

Hunter, C.A., and S.A. Jones. 2015. IL-6 as a keystone cytokine in health and disease. *Nat. Immunol.* 16:448–457. https://doi.org/10.1038/ni.3153

Huyghe, J., D. Priem, and M.J.M. Bertrand. 2023. Cell death checkpoints in the TNF pathway. *Trends Immunol.* 44:628–643. https://doi.org/10.1016/j.it.2023.05.007

Jaco, I., A. Annibaldi, N. Lalaoui, R. Wilson, T. Tenev, L. Laurien, C. Kim, K. Jamal, S. Wicky John, G. Liccardi, et al. 2017. MK2 phosphorylates RIPK1 to prevent TNF-induced cell death. *Mol. Cell*. 66:698–710.e5. https://doi.org/10.1016/j.molcel.2017.05.003

Jaffer, U., R.G. Wade, and T. Gourlay. 2010. Cytokines in the systemic inflammatory response syndrome: A review. *HSR Proc. Intensive Care Cardiovasc. Anesth.* 2:161–175

Jetton, D., H.I. Muendlein, W.M. Connolly, Z. Magri, I. Smirnova, R. Batorsky, J. Mecsas, A. Degterev, and A. Poltorak. 2024. Non-canonical autophosphorylation of RIPK1 drives timely pyroptosis to control Yersinia infection. *Cell Rep.* 43:114641. https://doi.org/10.1016/j.celrep.2024.114641

Kaiser, W.J., L.P. Daley-Bauer, R.J. Thapa, P. Mandal, S.B. Berger, C. Huang, A. Sundararajan, H. Guo, L. Roback, S.H. Speck, et al. 2014. RIP1 suppresses innate immune necrotic as well as apoptotic cell death during mammalian parturition. *Proc. Natl. Acad. Sci. USA*. 111:7753–7758. https://doi.org/10.1073/pnas.1401857111

Kist, M., L.G. Kőműves, T. Goncharov, D.L. Dugger, C. Yu, M. Roose-Girma, K. Newton, J.D. Webster, and D. Vucic. 2021. Impaired RIPK1 ubiquitination sensitizes mice to TNF toxicity and inflammatory cell death. *Cell Death Differ.* 28:985–1000. https://doi.org/10.1038/s41418-020-00629-3

Koerner, L., X. Li, E. Silnov, L. Laurien, and M. Pasparakis. 2025. RIPK1 autophosphorylation at S161 mediates cell death and inflammation. *J. Exp. Med.* https://doi.org/10.1084/jem.20250279

Lalaoui, N., S.E. Boyden, H. Oda, G.M. Wood, D.L. Stone, D. Chau, L. Liu, M. Stoffels, T. Kratina, K.E. Lawlor, et al. 2020. Mutations that prevent caspase cleavage of RIPK1 cause autoinflammatory disease. *Nature*. 577:103–108. https://doi.org/10.1038/s41586-019-1828-5

Laurien, L., M. Nagata, H. Schünke, T. Delanghe, J.L. Wiederstein, S. Kumari, R. Schwarzer, T. Corona, M. Krüger, M.J.M. Bertrand, et al. 2020. Autophosphorylation at serine 166 regulates RIP kinase 1-mediated cell death and inflammation. *Nat. Commun.* 11:1747. https://doi.org/10.1038/s41467-020-15466-8

Leuchtmann, A.B., R. Furrer, S.A. Steurer, K. Schneider-Heieck, B. Karrer-Cardel, Y. Sagot, and C. Handschin. 2022. Interleukin-6 potentiates endurance training adaptation and improves functional capacity in old mice. *J. Cachexia Sarcopenia Muscle*. 13:1164–1176. https://doi.org/10.1002/jcsm.12949

Li, W.L., X. Cheng, X.H. Tan, J.S. Zhang, Y.S. Sun, L. Chen, and X. Yang. 2005. Endothelial cell-specific expression of Cre recombinase in transgenic mice. *Yi Chuan Xue Bao*. 32:909–915.

Li, X., M. Zhang, X. Huang, W. Liang, G. Li, X. Lu, Y. Li, H. Pan, L. Shi, H. Zhu, et al. 2020. Ubiquitination of RIPK1 regulates its activation mediated by TNFR1 and TLRs signaling in distinct manners. *Nat. Commun.* 11:6364. https://doi.org/10.1038/s41467-020-19935-y

Libert, C., A. Vink, P. Coulie, P. Brouckaert, B. Everaerdt, J. Van Snick, and W. Fiers. 1992. Limited involvement of interleukin-6 in the pathogenesis of lethal septic shock as revealed by the effect of monoclonal antibodies against interleukin-6 or its receptor in various murine models. *Eur. J. Immunol.* 22:2625–2630. https://doi.org/10.1002/eji.1830221023

Liu, J., W. Li, X. Jin, F. Lin, J. Han, and Y. Zhang. 2023. Optimal tagging strategies for illuminating expression profiles of genes with different abundance in zebrafish. *Commun. Biol.* 6:1300. https://doi.org/10.1038/s42003-023-05686-1

Liu, Z., R.J. Simpson, and C. Cheers. 1992. Recombinant interleukin-6 protects mice against experimental bacterial infection. *Infect. Immun.* 60:4402–4406. https://doi.org/10.1128/iai.60.10.4402-4406.1992

McQuade, T., Y. Cho, and F.K.-M. Chan. 2013. Positive and negative phosphorylation regulates RIP1- and RIP3-induced programmed necrosis. *Biochem. J.* 456:409–415. https://doi.org/10.1042/BJ20130860

Menon, M.B., J. Gropengießer, J. Fischer, L. Novikova, A. Deuretzbacher, J. Lafera, H. Schimmeck, N. Czymmeck, N. Ronkina, A. Kotlyarov, et al. 2017. p38(MAPK)/MK2-dependent phosphorylation controls cytotoxic RIPK1 signalling in inflammation and infection. *Nat. Cell Biol.* 19:1248–1259. https://doi.org/10.1038/ncb3614

Mifflin, L., D. Ofengeim, and J. Yuan. 2020. Receptor-interacting protein kinase 1 (RIPK1) as a therapeutic target. *Nat. Rev. Drug Discov.* 19:553–571. https://doi.org/10.1038/s41573-020-0071-y

Mulé, J.J., M.C. Custer, W.D. Travis, and S.A. Rosenberg. 1992. Cellular mechanisms of the antitumor activity of recombinant IL-6 in mice. *J. Immunol.* 148:2622–2629.

Newton, K., D.L. Dugger, A. Maltzman, J.M. Greve, M. Hedehus, B. Martin-McNulty, R.A.D. Carano, T.C. Cao, N. van Bruggen, L. Bernstein, et al. 2016. RIPK3 deficiency or catalytically inactive RIPK1 provides greater benefit than MLKL deficiency in mouse models of inflammation and tissue injury. *Cell Death Differ.* 23:1565–1576. https://doi.org/10.1038/cdd.2016.46

Newton, K., D.L. Dugger, K.E. Wickliffe, N. Kapoor, M.C. de Almagro, D. Vucic, L. Komuves, R.E. Ferrando, D.M. French, J. Webster, et al. 2014. Activity of protein kinase RIPK3 determines whether cells die by necroptosis or apoptosis. *Science*. 343:1357–1360. https://doi.org/10.1126/science.1249361

Newton, K., K.E. Wickliffe, D.L. Dugger, A. Maltzman, M. Roose-Girma, M. Dohse, L. Kőműves, J.D. Webster, and V.M. Dixit. 2019. Cleavage of RIPK1 by caspase-8 is crucial for limiting apoptosis and necroptosis. *Nature*. 574:428–431. https://doi.org/10.1038/s41586-019-1548-x

Polykratis, A., N. Hermance, M. Zelic, J. Roderick, C. Kim, T.-M. Van, T.H. Lee, F.K.M. Chan, M. Pasparakis, and M.A. Kelliher. 2014. Cutting edge: RIPK1 kinase inactive mice are viable and protected from TNF-induced necroptosis in vivo. *J. Immunol.* 193:1539–1543. https://doi.org/10.4049/jimmunol.1400590

Sacco, F., S.J. Humphrey, J. Cox, M. Mischnik, A. Schulte, T. Klabunde, M. Schäfer, and M. Mann. 2016. Glucose-regulated and drug-perturbed phosphoproteome reveals molecular mechanisms controlling insulin secretion. *Nat. Commun.* 7:13250. https://doi.org/10.1038/ncomms13250

Schwarzer, R., H. Jiao, L. Wachsmuth, A. Tresch, and M. Pasparakis. 2020a. FADD and caspase-8 regulate gut homeostasis and inflammation by controlling MLKL- and GSDMD-mediated death of intestinal epithelial cells. *Immunity*. 52:978–993.e6. https://doi.org/10.1016/j.immuni.2020.04.002

Schwarzer, R., L. Laurien, and M. Pasparakis. 2020b. New insights into the regulation of apoptosis, necroptosis, and pyroptosis by receptor interacting protein kinase 1 and caspase-8. *Curr. Opin. Cell Biol.* 63:186–193. https://doi.org/10.1016/j.ceb.2020.02.004

Shutinoski, B., N.A. Alturki, D. Rijal, J. Bertin, P.J. Gough, M.G. Schlossmacher, and S. Sad. 2016. K45A mutation of RIPK1 results in poor necroptosis and cytokine signaling in macrophages, which impacts inflammatory responses in vivo. *Cell Death Differ.* 23:1628–1637. https://doi.org/10.1038/cdd.2016.51

Sun, L., H. Wang, Z. Wang, S. He, S. Chen, D. Liao, L. Wang, J. Yan, W. Liu, X. Lei, and X. Wang. 2012. Mixed lineage kinase domain-like protein mediates necrosis signaling downstream of RIP3 kinase. *Cell.* 148: 213–227. https://doi.org/10.1016/j.cell.2011.11.031

Sundgren-Andersson, A.K., P. Ostlund, and T. Bartfai. 1998. IL-6 is essential in TNF-alpha-induced fever. *Am. J. Physiol.* 275:R2028–R2034. https://doi.org/10.1152/ajpregu.1998.275.6.R2028

Tang, Y., H. Tu, J. Zhang, X. Zhao, Y. Wang, J. Qin, and X. Lin. 2019. K63-linked ubiquitination regulates RIPK1 kinase activity to prevent cell death during embryogenesis and inflammation. *Nat. Commun.* 10:4157. https://doi.org/10.1038/s41467-019-12033-8

Tao, P., J. Sun, Z. Wu, S. Wang, J. Wang, W. Li, H. Pan, R. Bai, J. Zhang, Y. Wang, et al. 2020. A dominant autoinflammatory disease caused by non-cleavable variants of RIPK1. *Nature.* 577:109–114. https://doi.org/10.1038/s41586-019-1830-y

Tracey, K.J., B. Beutler, S.F. Lowry, J. Merryweather, S. Wolpe, I.W. Milsark, R.J. Hariri, T.J. Fahey 3rd, A. Zentella, J.D. Albert, et al. 1986. Shock and tissue injury induced by recombinant human cachectin. *Science.* 234: 470–474. https://doi.org/10.1126/science.3764421

Tu, H., Y. Tang, J. Zhang, L. Cheng, D. Joo, X. Zhao, and X. Lin. 2021. Linear ubiquitination of RIPK1 on Lys612 regulates systemic inflammation via preventing cell death. *J. Immunol.* 207:602–612. https://doi.org/10.4049/jimmunol.2100299

Tu, H., W. Xiong, J. Zhang, X. Zhao, and X. Lin. 2022. Tyrosine phosphorylation regulates RIPK1 activity to limit cell death and inflammation. *Nat. Commun.* 13:6603. https://doi.org/10.1038/s41467-022-34080-4

Van Antwerp, D.J., S.J. Martin, T. Kafri, D.R. Green, and I.M. Verma. 1996. Suppression of TNF-alpha-induced apoptosis by NF-kappaB. *Science.* 274:787–789. https://doi.org/10.1126/science.274.5288.787

Voravuthikunchai, S.P., and A. Lee. 1987. Cecectomy causes long-term reduction of colonization resistance in the mouse gastrointestinal tract. *Infect. Immun.* 55:995–999. https://doi.org/10.1128/iai.55.4.995-999.1987

Wang, L., F. Du, and X. Wang. 2008. TNF-alpha induces two distinct caspase-8 activation pathways. *Cell.* 133:693–703. https://doi.org/10.1016/j.cell.2008.03.036

Wang, Y., M. Nakayama, M.E. Pitulescu, T.S. Schmidt, M.L. Bochenek, A. Sakakibara, S. Adams, A. Davy, U. Deutsch, U. Lüthi, et al. 2010. Ephrin-B2 controls VEGF-induced angiogenesis and lymphangiogenesis. *Nature.* 465:483–486. https://doi.org/10.1038/nature09002

Weisel, K., S. Berger, K. Thorn, P.C. Taylor, C. Peterfy, H. Siddall, D. Tompson, S. Wang, E. Quattrocchi, S.W. Burriss, et al. 2021a. A randomized, placebo-controlled experimental medicine study of RIPK1 inhibitor GSK2982772 in patients with moderate to severe rheumatoid arthritis. *Arthritis Res. Ther.* 23:85. https://doi.org/10.1186/s13075-021-02468-0

Weisel, K., N. Scott, S. Berger, S. Wang, K. Brown, M. Powell, M. Broer, C. Watts, D.J. Tompson, S.W. Burriss, et al. 2021b. A randomised, placebo-controlled study of RIPK1 inhibitor GSK2982772 in patients with active ulcerative colitis. *BMJ Open Gastroenterol.* 8:e000680. https://doi.org/10.1136/bmjgast-2021-000680

Wu, J., T. Ai, P. He, Q. Shi, Y. Li, Z. Zhang, M. Chen, Z. Huang, S. Wu, W. Chen, and J. Han. 2024a. Cecal necroptosis triggers lethal cardiac dysfunction in TNF-induced severe SIRS. *Cell Rep.* 43:114778. https://doi.org/10.1016/j.celrep.2024.114778

Wu, W., X. Wang, N. Berleth, J. Deitersen, N. Wallot-Hieke, P. Böhler, D. Schlütermann, F. Stuhldreier, J. Cox, K. Schmitz, et al. 2020. The autophagy-initiating kinase ULK1 controls RIPK1-mediated cell death. *Cell Rep.* 31:107547. https://doi.org/10.1016/j.celrep.2020.107547

Wu, X., X. Zhao, F. Li, Y. Wang, Y. Ou, H. Zhang, X. Li, X. Wu, L. Wang, M. Li, et al. 2024b. MLKL-mediated endothelial necroptosis drives vascular damage and mortality in systemic inflammatory response syndrome. *Cell Mol. Immunol.* 21:1309–1321. https://doi.org/10.1038/s41423-024-01217-y

Xie, T., W. Peng, Y. Liu, C. Yan, J. Maki, A. Degterev, J. Yuan, and Y. Shi. 2013. Structural basis of RIP1 inhibition by necrostatins. *Structure.* 21: 493–499. https://doi.org/10.1016/j.str.2013.01.016

Zelic, M., J.E. Roderick, J.A. O'Donnell, J. Lehman, S.E. Lim, H.P. Janardhan, C.M. Trivedi, M. Pasparakis, and M.A. Kelliher. 2018. RIP kinase 1-dependent endothelial necroptosis underlies systemic inflammatory response syndrome. *J. Clin. Invest.* 128:2064–2075. https://doi.org/10.1172/JCI96147

Zhang, D.-W., J. Shao, J. Lin, N. Zhang, B.-J. Lu, S.-C. Lin, M.-Q. Dong, and J. Han. 2009. RIP3, an energy metabolism regulator that switches TNF-induced cell death from apoptosis to necrosis. *Science.* 325:332–336. https://doi.org/10.1126/science.1172308

Zhang, X., J.P. Dowling, and J. Zhang. 2019a. RIPK1 can mediate apoptosis in addition to necroptosis during embryonic development. *Cell Death Dis.* 10:245. https://doi.org/10.1038/s41419-019-1490-8

Zhang, X., H. Zhang, C. Xu, X. Li, M. Li, X. Wu, W. Pu, B. Zhou, H. Wang, D. Li, et al. 2019b. Ubiquitination of RIPK1 suppresses programmed cell death by regulating RIPK1 kinase activation during embryogenesis. *Nat. Commun.* 10:4158. https://doi.org/10.1038/s41467-019-11839-w

Zhang, Y., X. Chen, C. Gueydan, and J. Han. 2018. Plasma membrane changes during programmed cell deaths. *Cell Res.* 28:9–21. https://doi.org/10.1038/cr.2017.133

Zhang, Y., K. Huang, Y. Zhang, T. Han, L. Li, C. Ruan, Y.-H. Sun, W. Shi, W. Han, S.-Q. Wu, et al. 2021. A unique death pathway keeps RIPK1 D325A mutant mice in check at embryonic day 10.5. *PLoS Biol.* 19:e3001304. https://doi.org/10.1371/journal.pbio.3001304

Zhang, Y., S.S. Su, S. Zhao, Z. Yang, C.-Q. Zhong, X. Chen, Q. Cai, Z.-H. Yang, D. Huang, R. Wu, and J. Han. 2017. RIP1 autophosphorylation is promoted by mitochondrial ROS and is essential for RIP3 recruitment into necrosome. *Nat. Commun.* 8:14329. https://doi.org/10.1038/ncomms14329

Zhong, C., Q. Yin, Z. Xie, M. Bai, R. Dong, W. Tang, Y.-H. Xing, H. Zhang, S. Yang, L.-L. Chen, et al. 2015. CRISPR-Cas9-Mediated genetic screening in mice with haploid embryonic stem cells carrying a guide RNA library. *Cell Stem Cell.* 17:221–232. https://doi.org/10.1016/j.stem.2015.06.005

Supplemental material

A

Ripk1$^{S161E/+}$ ♂ × *Ripk1*$^{S161E/+}$ ♀

Genotype	+/+	S161E/+	S161E/S161E	Total
Expected	8	17	8	33
Actual (weaning)	8	16	9	

B

Ripk1$^{S161N/+}$ ♂ × *Ripk1*$^{S161N/+}$ ♀

Genotype	+/+	S161N/+	S161N/S161N	Total
Expected	13	28	13	55
Actual (weaning)	15	28	12	

C

Ripk1$^{S161A/+}$ ♂ × *Ripk1*$^{S161A/+}$ ♀

Genotype	+/+	S161A/+	S161A/S161A	Total
Expected	17	35	17	69
Actual (weaning)	18	36	15	

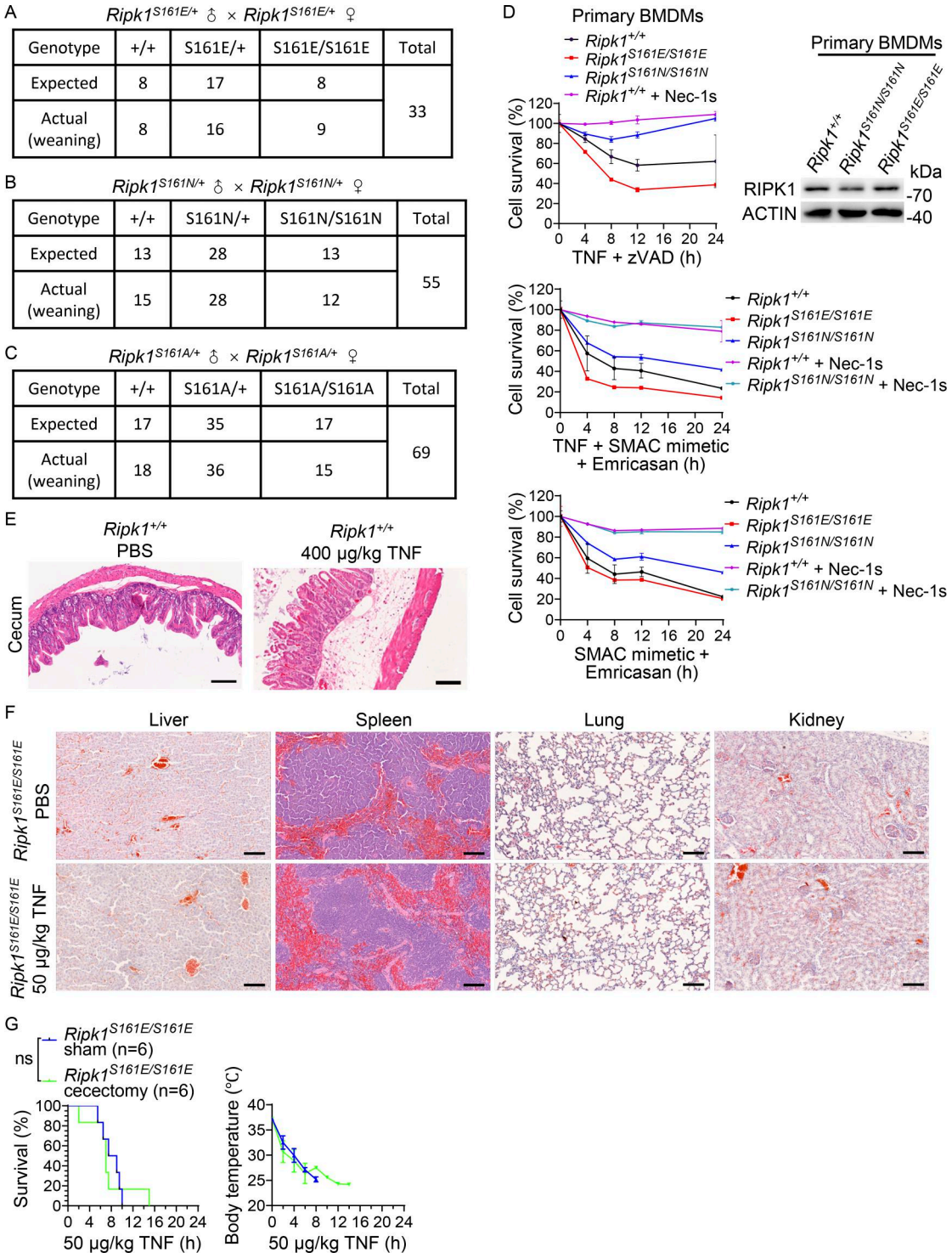

Figure S1. **S161E mutation sensitizes the cecum to TNF-induced damage. (A–C)** Genetic analyses of offspring from intercrosses of *Ripk1*$^{S161E/+}$, *Ripk1*$^{S161N/+}$, and *Ripk1*$^{S161A/+}$ parents, respectively. **(D)** Primary BMDMs from *Ripk1*$^{+/+}$, *Ripk1*$^{S161N/S161N}$, or *Ripk1*$^{S161E/S161E}$ mice (three littermate 8- to 12-wk-old male mice of each genotype) were treated with TNF (10 ng/ml) + zVAD (20 μM), TNF (20 ng/ml) + SMAC mimetic (1 μM) + Emricasan (5 μM), or SMAC mimetic (1 μM) + Emricasan (5 μM) for the indicated time points with or without Nec-1s (10 μM). Cell survival was measured. Data are presented as mean ± SD. Cell lysates of nontreated primary BMDMs were analyzed by immunoblotting to detect proteins as indicated. **(E)** Representative H&E staining images of ceca from *Ripk1*$^{+/+}$ mice after TNF treatment for 6 h (400 μg/kg, i.v.) or PBS. Three 8- to 12-wk-old littermate male mice were used for each treatment. Scale bars, 100 μm. **(F)** Representative H&E staining images of livers, spleens, lungs, and kidneys from *Ripk1*$^{S161E/S161E}$ mice after PBS or TNF treatment for 6 h (50 μg/kg, i.v.). Three 8- to 12-wk-old littermate male mice were used for each treatment. Scale bars, 100 μm. **(G)** 6- to 8-wk-old male littermate mice were treated with or without cecectomy and then injected with TNF after 4 wk (50 μg/kg i.v.). Survival curve is presented as a Kaplan–Meier plot, and the log-rank (Mantel–Cox) test (two-sided) is performed to determine statistical significance. ns, $P \geq 0.05$. Data of body temperature are presented as mean ± SD. The above experiments were independently performed twice. Source data are available for this figure: SourceData FS1.

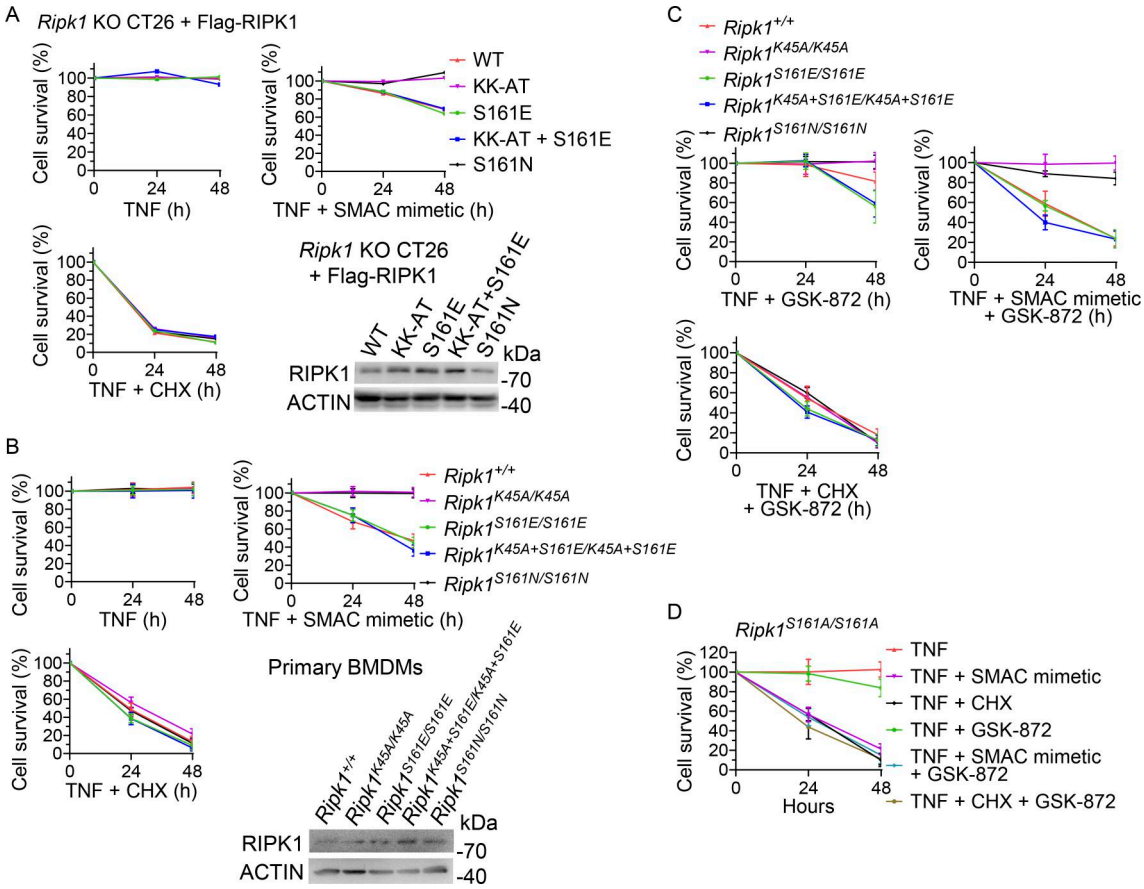

Figure S2. **S161 phosphorylation is required for TNF-induced RIPK1 kinase–dependent apoptosis, but not RIPK1 kinase–independent apoptosis, in CT26 cells and in primary BMDMs. (A–D)** *Ripk1*-deficient CT26 cells reconstituted with Flag-RIPK1 WT or mutants (A) and primary BMDMs from three mice of each genotype as indicated (B–D) were treated with TNF (10 ng/ml), TNF (10 ng/ml) + SMAC mimetic (1 µM), and TNF (10 ng/ml) + CHX (1 µg/ml), respectively, in the presence or absence of GSK-872 for the indicated time points. All mice were 8- to 12-wk-old male littermates. Cell survival was measured. Data are presented as mean ± SD. Cell lysates of nontreated cells were analyzed by immunoblotting to detect proteins as indicated. The above experiments were independently performed twice. Source data are available for this figure: SourceData FS2.

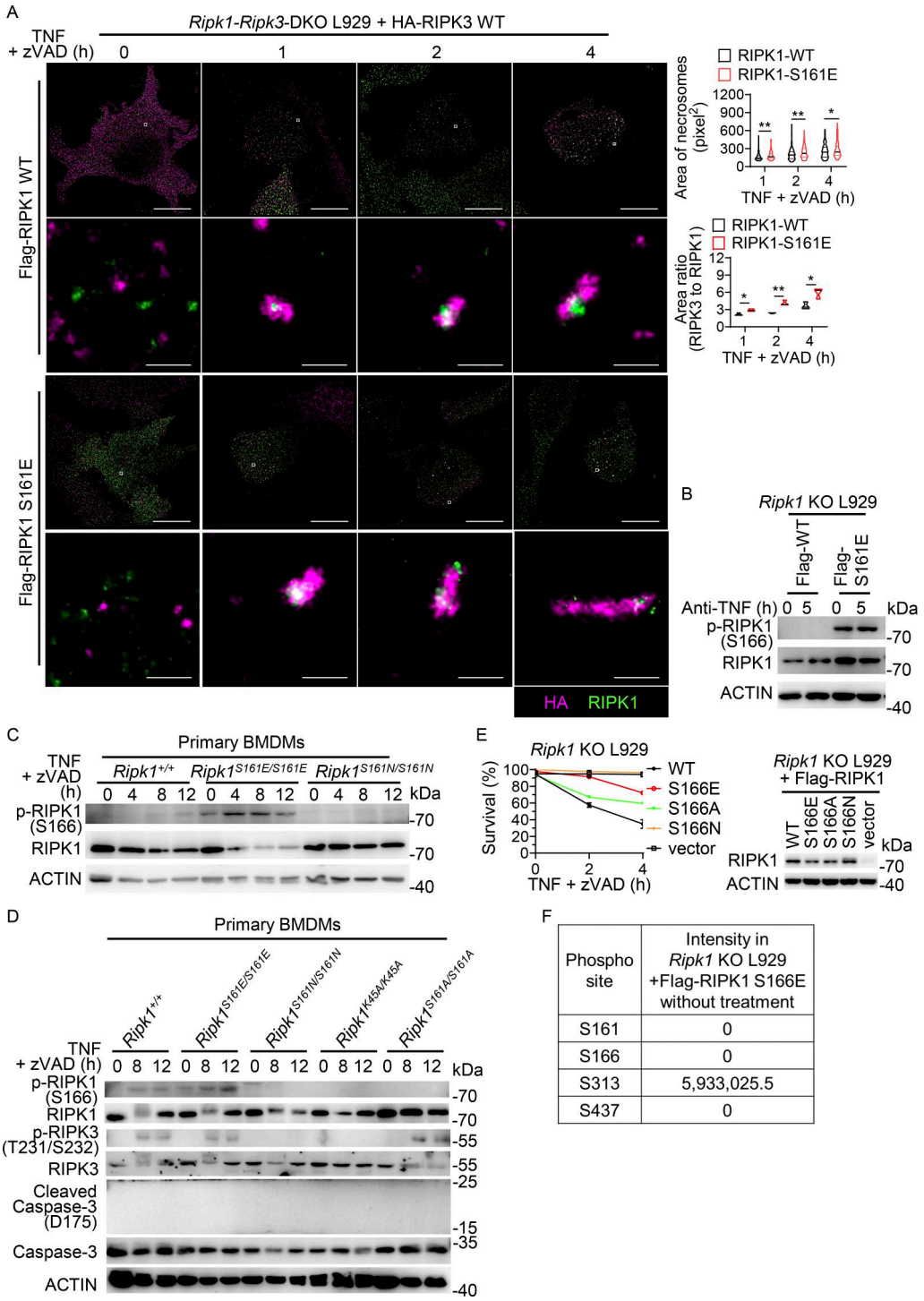

Phospho site	Intensity in *Ripk1* KO L929 +Flag-RIPK1 S166E without treatment
S161	0
S166	0
S313	5,933,025.5
S437	0

Figure S3. **RIPK1 phosphorylation at S161 occurs prior to RIPK1 phosphorylation at S166. (A)** *Ripk1* and *Ripk3* double-deficient L929 cells were reconstituted with Flag-RIPK1 WT or S161E mutant and HA-RIPK3 WT and then treated with TNF (10 ng/ml) + zVAD (20 μM) for 1, 2, or 4 h. Representative STORM images from two independent experiments of RIPK1 (green) and RIPK3 (purple) in L929 cells with or without treatment are shown. Scale bars, 10 μm for the first and third rows and 200 nm for the second and fourth rows from the top. Area of necrosomes formed after treatment and area ratios of RIPK3 to RIPK1 were analyzed using ImageJ. P values are determined by a two-tailed, unpaired *t* test. **P < 0.01; *P < 0.05. **(B)** *Ripk1*-deficient L929 cells were reconstituted with Flag-RIPK1 WT or S161E mutant and then treated with anti-TNF antibody (1 μg/ml) for the indicated time points. Cell lysates were analyzed by immunoblotting to detect proteins as indicated. **(C and D)** Cell lysates of TNF (10 ng/ml) + zVAD (20 μM)-treated primary BMDMs from littermate *Ripk1*$^{+/+}$, *Ripk1*$^{S161E/S161E}$, *Ripk1*$^{S161N/S161N}$, *Ripk1*$^{S161A/S161A}$, and *Ripk1*$^{K45A/K45A}$ male mice were analyzed by immunoblotting to detect proteins as indicated. **(E)** *Ripk1* KO L929 cells were reconstituted with WT RIPK1 or RIPK1 mutants and then treated with TNF (10 ng/ml) + zVAD (20 μM) for the indicated time points. Cell survival was measured. Cell lysates of nontreated cells were analyzed by immunoblotting to detect proteins as indicated. Data are presented as mean ± SD of triplicate. **(F)** Intensities of RIPK1 phosphorylation sites measured by LC–MS/MS. Samples were *Ripk1* KO L929 cells reconstituted with RIPK1 S166E mutant without treatment. The above experiments were independently performed twice. Source data are available for this figure: SourceData FS3.

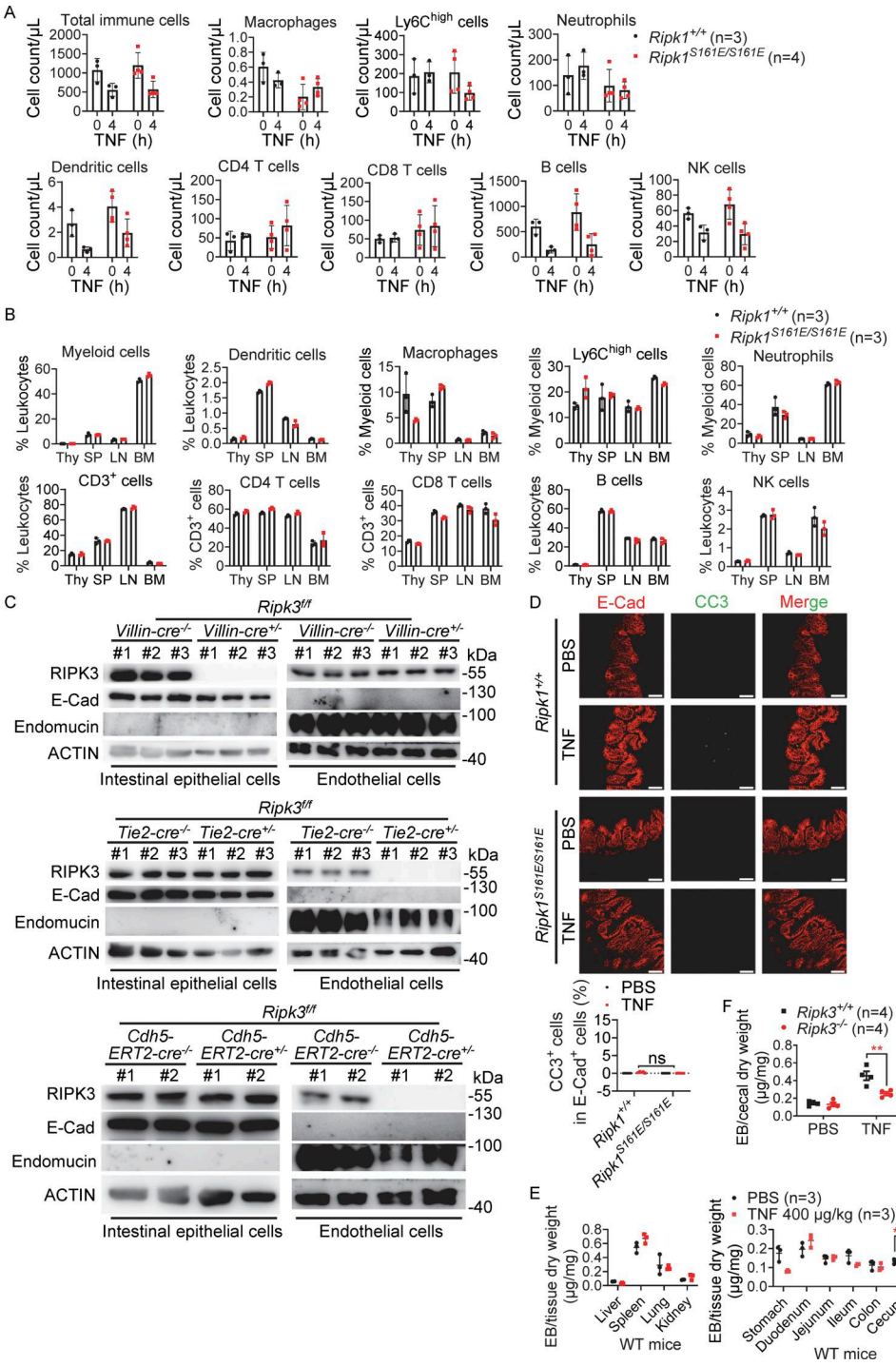

Figure S4. **IEC and EC necroptosis are triggers of TNF-induced death of *Ripk1*$^{S161E/S161E}$ mice. (A)** Flow cytometry analysis of counts of total immune cells and different subsets in the peripheral blood of 8- to 12-wk-old male littermate *Ripk1*$^{+/+}$ and *Ripk1*$^{S161E/S161E}$ mice after TNF injection (50 μg/kg, i.v.) at the indicated time points. **(B)** Immune cell compositions of the thymus (Thy), spleen (SP), lymph node (LN), and bone marrow (BM) of untreated *Ripk1*$^{+/+}$ and *Ripk1*$^{S161E/S161E}$ mice were analyzed using flow cytometry. All mice were 8- to 12-wk-old male littermates. The number of mice used was as indicated. **(C)** Cecal IECs and ECs were isolated from male *Ripk3*$^{f/f}$ *Villin-cre*$^{+/-}$ mice, *Ripk3*$^{f/f}$ *Tie2-cre*$^{+/-}$ mice, and their littermate *Ripk3*$^{f/f}$ mice, and tamoxifen-treated male *Ripk3*$^{f/f}$ *Cdh5-ERT2-cre*$^{+/-}$ mice and their littermate *Ripk3*$^{f/f}$ mice, respectively. RIPK3 expression in the cell lysates was examined by immunoblotting. E-cadherin and endomucin were used as markers for IECs and ECs, respectively. Each number represents one mouse. The above experiments were independently performed twice. **(D)** Representative immunofluorescence staining images of ceca from five mice of each indicated genotype after TNF treatment for 6 h (50 μg/kg, i.v.). All mice were 8- to 12-wk-old male littermates. E-Cad (red), cleaved caspase-3 D175 (CC3, green). Scale bars, 50 μm. Percentages of CC3$^+$ cells in E-Cad$^+$ cells were quantified using ImageJ. Data are presented as mean ± SD. P values are determined by a two-tailed, unpaired *t* test. ns, P ≥ 0.05. **(E and F)** 8- to 12-wk-old littermate male WT mice (A) and *Ripk3*$^{-/-}$ mice (B) were injected with PBS or TNF (400 μg/kg, i.v.) for 4 h and then EB (0.5 mg/mouse) for 20 min. Organs were collected, and the amount of EB extracted from the organs was measured by spectrophotometry. Data are presented as mean ± SD. P values are determined by a two-tailed, unpaired *t* test. **P < 0.01. Source data are available for this figure: SourceData FS4.

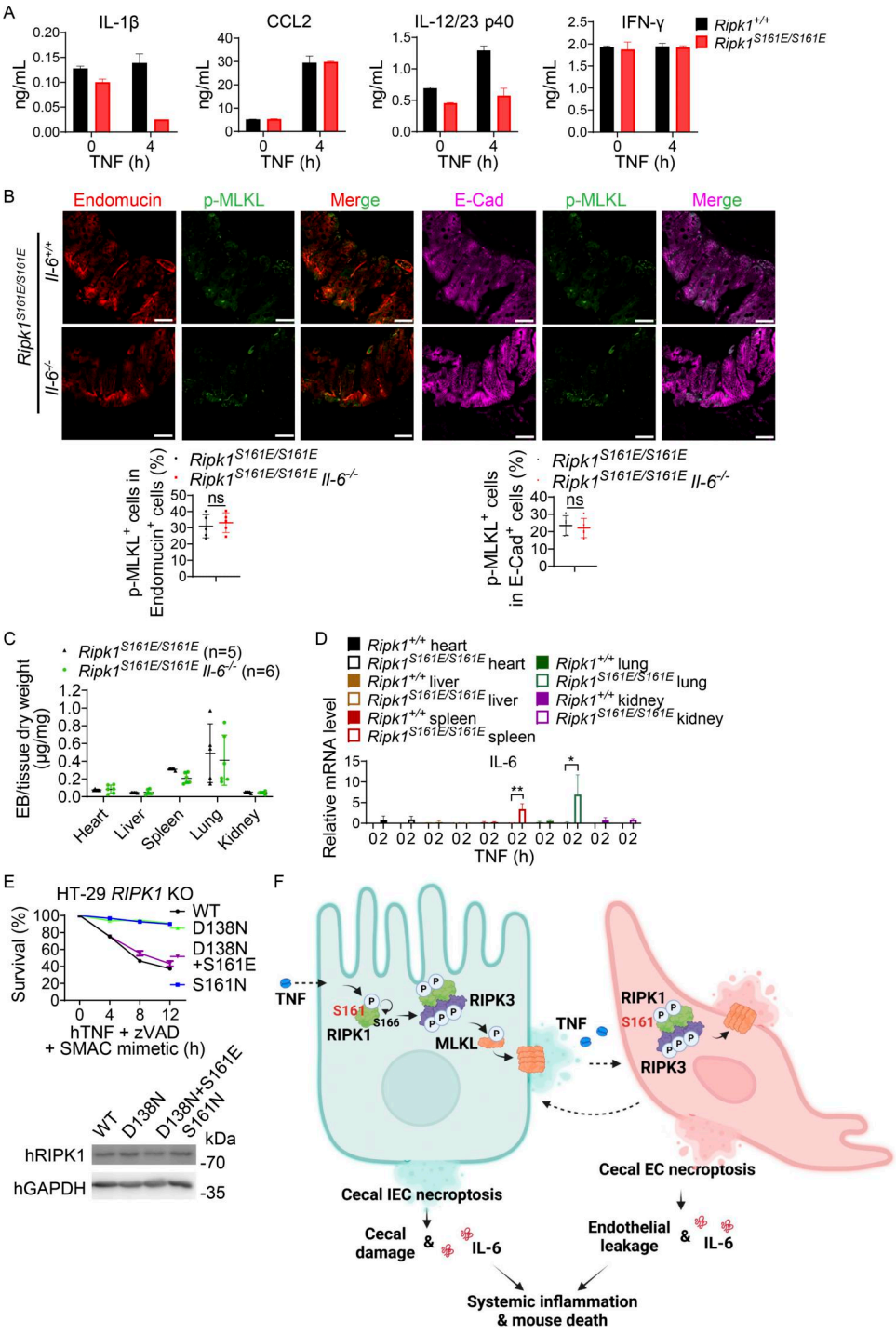

Figure S5. **Necroptosis raises IL-6 levels in the circulation, which facilitates the death of *Ripk1*$^{S161E/S161E}$ mice. (A)** 8- to 12-wk-old male littermate *Ripk1*$^{+/+}$ and *Ripk1*$^{S161E/S161E}$ mice (n = 3) were i.v. injected with TNF (50 μg/kg). At the indicated time points, serum samples were collected for ELISA analysis of IL-1β, CCL2, IL-12/23 p40, and IFN-γ. **(B)** Representative immunofluorescence staining images of ceca from five 8- to 12-wk-old male littermate mice of each indicated genotype after TNF treatment for 6 h (50 μg/kg, i.v.). Endomucin, red; p-MLKL, green; E-Cad, purple. Scale bars, 50 μm. Percentages of p-MLKL$^+$ cells in Endomucin$^+$ cells or E-Cad$^+$ cells were quantified using ImageJ. Data are presented as mean ± SD. P values are determined by a two-tailed, unpaired t test. ns, P ≥ 0.05. **(C)** 8- to 12-wk-old male littermate mice of the indicated genotypes were treated with TNF for 4 h (50 μg/kg, i.v.) and then EB (0.5 mg/mouse) for 20 min. Organs were collected, and the amount of EB extracted from the organs was measured by spectrophotometry. **(D)** Quantitative RT-PCR analysis of *Il-6* mRNA levels in organs of mice (n = 6) after TNF injection (50 μg/kg, i.v.) at the indicated time points. All mice were 8- to 12-wk-old male littermates. Data are presented as mean ± SD. P values are determined by a two-tailed, unpaired t test. *P < 0.05; **P < 0.01. **(E)** *RIPK1*-deficient HT-29 cells were reconstituted with Flag-hRIPK1 WT or mutants (D138N, D138N + S161E, and S161N) and then treated with hTNF (30 ng/ml) + zVAD (20 μM) + SMAC mimetic (100 nM) for the indicated time points. Cell survival was measured. Data are presented as mean ± SD of triplicate. Cell lysates were analyzed by immunoblotting. The above experiments were independently performed twice. **(F)** A graphic model for the functions and mechanisms of RIPK1 S161 phosphorylation in TNF-induced SIRS, created in BioRender. Msf, (2025) https://BioRender.com/w9bzp6q. Source data are available for this figure: SourceData FS5.